Key Structural Kinetics for Carbon Effects on the Performance and Durability of Pt/Carbon Cathode Catalysts in Polymer Electrolyte Fuel Cells Characterized by In Situ Time-Resolved X-ray Absorption Fine Structure

doi: 10.1021/acs.jpcc.6b08569

Key Structural Kinetics for Carbon Effects on the Performance and Durability of Pt/Carbon Cathode Catalysts in Polymer Electrolyte Fuel Cells Characterized by *In Situ* Time-Resolved XAFS

Takuma Kaneko,[†] Gabor Samjeské,[†] Shin-ichi Nagamatsu,[†] Kotaro Higashi,[†] Oki Sekizawa,[†] Shinobu Takao,[†] Takashi Yamamoto,[‡] Xiao Zhao,[†] Tomohiro Sakata,[†] Tomoya Uruga,[†,§] and Yasuhiro Iwasawa[†,#]*

[†] Innovation Research Center for Fuel Cells, The University of Electro-Communications, Chofugaoka, Chofu, Tokyo 182-8585, Japan

[‡] Department of Mathematical and Material Sciences, The University of Tokushima, Minamijosanjima, Tokushima 770-8502, Japan

[§] Japan Synchrotron Radiation Research Institute, SPring-8, Sayo, Hyogo 679-5198, Japan

[#] Graduate School of Infotmatics and Engineering, The University of Electro-Communications, Chofugaoka, Chofu, Tokyo 182-8585, Japan

ABSTRACT. The structural kinetics (rate constants for electronic and structural transformations) of the Pt charging/discharging, Pt-Pt bond dissociation/reformation and Pt-O bond formation/dissociation of Pt/KB, Pt/AB and Pt/MWCNT cathode catalysts in PEFC MEAs under transient potential operations (0.4 V_{RHE} →1.4 V_{RHE} →0.4 V_{RHE}) has been studied by *in situ*/*operando* time-resolved QXAFS (100 ms/spectrum), while measuring electrochemical currents/charges in the MEAs under the potential operations. From the systematic QXAFS analysis for potential-dependent surface structures and rate constants (k and k') for the transformations of Pt nanoparticles under the operations (0.4 V_{RHE} →1.4 V_{RHE} and 1.4 V_{RHE} →0.4 V_{RHE}), respectively, we have found the structural kinetics ($k'_{Pt\text{-}O}$ and $k'_{valence}$) controlling the oxygen reduction reaction (ORR) activity and also the structural kinetics ($k'_{Pt\text{-}Pt}/k_{Pt\text{-}Pt}$) reflecting the durability of the cathode catalysts. The relaxation time of the Pt-Pt bond reformation and Pt-O bond dissociation processes in the activated MEAs was also suggested to predict the relative durability of the similar kinds of cathode catalysts. The *in situ* time-resolved XAFS analysis provided direct information on the key structural kinetics of the Pt/C catalysts themselves for thorough understanding of the cathode catalysis toward PEFC improvement.

1. INTRODUCTION

In these decades polymer electrolyte fuel cell (PEFC) has received much attention as one of the most efficient clean energy generation systems, bringing zero emissions into reality in the future, particularly for automotive applications due to high power density at low temperatures. In December 2014 TOYOTA launched the world's first commercially available hydrogen fuel-cell vehicle “MIRAI” and in March 2016 HONDA also launched the commercial hydrogen fuel-cell vehicle “CLARITY FUEL CELL” by using carbon-supported Pt-based nanoparticle catalysts (Pt/C) as cathode in membrane electrode assembly (MEA) as an active unit of PEFC. This is an epoch-making technology, but for widely spread commercialization of PEFC vehicles including cars for business use, further improvements of the oxygen reduction reaction (ORR) activity and durability of Pt/C cathode electrocatalysts, which remarkably reduce the cost of PEFC stacking, are indispensable.[1-23] There are a lot of fundamental researches required to benefit from the ultimate potential of PEFCs. In particular, our understanding of the structural kinetics and dynamic behaviors of cathode catalysts relevant to molecular-level mechanisms for the performance and long-term durability of MEAs under the harsh PEFC operating conditions is still incomplete, which must be understood more thoroughly for development of next-generation PEFCs for automobiles.

However, there are few suitable *in situ* analysis methods to elucidate the transformations of structures and chemical states of cathode catalysts (structural kinetics) with nanometer dimensions inside MEA of PEFC at changing cathode voltages, while measuring the current/charge at the cathode, where the wet, heterogeneous and multiphasic reaction field involving catalyst nanoparticles, carbon supports, ionomers, water and fuel gases prevents spectroscopic techniques from *in situ* measuring the MEA cathode catalysts. X-ray absorption fine structure (XAFS) enabled *in situ* element-selective investigation on the local structures and oxidation states of a supported metal catalyst involving an intermediate structure during the course of catalytic reactions by using an *in situ* XAFS cell.[24-27] Nowadays *in situ* XAFS techniques are well recognized to be unique and powerful for structural and electronic characterizations of supported catalysts under working/operating conditions and more explicitly while analyzing the catalysis involving adsorption, diffusion and reactions (often called *operando*).[7,26-44] Tada et al. carried out successfully the world's first *in situ*/*operando* quick-XAFS (QXAFS) observation and thorough analysis of structural kinetics of a PEFC Pt/C cathode electrocatalyst in voltage cycling processes (0.4 V ⇆ 1.0 V vs RHE; hereinafter denoted as V_{RHE}).[45] They also developed *in situ* time-resolved QXAFS for PEFCs to elucidate the dynamic transformations

of structures and electronic states of Pt/C, Pt_3Co/C and Pt_3Ni/C cathode catalysts and to decide elementary steps and their rate constants for the chemical events at the cathode catalyst surfaces.[46-48]

We also reported that a Pt/Acetylene black (AB) cathode catalyst in PEFC MEA possesses eight times higher durability than a Pt/Ketjenblack (KB) cathode catalyst in view of maximum power density, and the high durability of the Pt/AB was referred to the higher tolerance to carbon degradation than the Pt/KB and the more stable environment of three phase (Pt-AB-ionomer) interface on AB.[37] *In situ* Pt L_{III}-edge XAFS analysis for both MEA Pt/KB and Pt/AB revealed that the surfaces of Pt nanoparticles in the cathode layers at 0.4 V_{RHE} were metallic and oxidized to form disordered $Pt^{2+}O$ layers with the Pt-O distance of 0.202 nm at 1.4 V_{RHE}.[37] The *in situ* XAFS analysis for the transformations of surface structures (Pt-Pt and Pt-O coordination numbers) and electronic states (Pt valence) of both Pt/KB and Pt/AB cathode catalysts in the increasing and decreasing voltage operation processes between 0.4 V_{RHE} and 1.4 V_{RHE} showed a hysteresis in the transformations.[37] These results did not evidence the reason and cause of the difference between the Pt/KB and Pt/AB catalysts in the durability, which attempted us to investigate the carbon effects on the performance and durability of Pt/C cathode catalysts in PEFCs by means of *in situ* time-resolved QXAFS technique at BL36XU beamline we constructed at SPring-8 for fuel cell characterizations under the operating conditions.[49]

In the present study we have examined the structural kinetics of the transformations (six elementary steps) of the Pt valence and Pt-Pt and Pt-O bonds of Pt/KB, Pt/AB and Pt/MWCNT (multi-walled carbon nanotube) in the transient response processes against the voltage jumps 0.4 $V_{RHE} \rightarrow$1.4 V_{RHE} and 1.4 $V_{RHE} \rightarrow$0.4 V_{RHE} and found the correlations between the rate constants and the ORR activity and also between the rate constants and the durability against triangular accelerated durability test (ADT) cycles by *in situ*/*operando* time-resolved QXAFS at 100 ms time-resolution, while measuring the current/charge of the PEFCs with Pt/KB, Pt/AB and Pt/MWCNT cathodes.

2. EXPERIMENTAL

2.1. MEA cathode catalysts and electrochemical measurements. The three kinds of Pt/C cathode catalysts, Pt/Ketjenblack (KB) (TEC10E50E, Tanaka Kikinzoku Kogyo), Pt/Acetylene black (AB) provided by a manufacturer and Pt/multi-walled carbon nanotube (MWCNT) (MWCNT: provided by a manufacturer), were used as cathode catalysts for PEFCs. The surface areas for the Pt/KB, Pt/AB and Pt/MWCNT were estimated to be 385, 437 and 182 m^2/g, respectively, and the mean pore diameters were estimated to be 9.6, 9.6 and 24.3 nm, respectively.[37] The MEAs used in this study were provided

by CHEMIX PEFC manufacturing co. Briefly, the cathode catalysts were coated onto MEAs, where Nafion NR-212 (Sigma-Aldrich) membrane was used as polymer electrolyte and Pd/KB (Tanaka Kikinzoku kogyo, TECPd(ONLY)E30; Pd: 29.9 wt%; 0.6 mg-Pd/cm^2) was used as an anode catalyst to avoid interference against XAFS measurements of the Pt/C cathodes. To avoid structural influences on MEA performances, all three types of cathode catalysts were hot-pressed onto the identical Nafion membrane, using identical binder and anode catalysts. The electrode catalyst areas in the MEAs were 3×3 cm^2, and the Pt loadings at the cathode in MEA for Pt/KB, Pt/AB and Pt/MWCNT were 0.6 mg-Pt cm^{-2} (Pt: 46.1 wt%) (TEC10E50E), 0.64 mg-Pt cm^{-2} (Pt: 40.0 wt%) and 0.6 mg-Pt cm^{-2} (Pt: 40.0 wt%), respectively. The prepared MEAs were sandwiched in a home-made XAFS cell using Viton® gaskets of 0.15 mm thickness, gas diffusion layers (GDL) and separator-plates (bipolar plates) with serpentine-shape type flow channels for both anode and cathode sides.

The cathode was connected as working electrode and the anode (hydrogen-fed) served as combined counter and reference electrode. All potentials are referred to this pseudo hydrogen reference electrode (RHE). The gas flows of H_2 (99.99999%; 150 sccm) for anode and N_2 (99.99995%; 300 sccm) or dry air (99.99995%; 900 sccm) for cathode were regulated by mass-flow controllers and were bubbled through humidifiers at 351 K. The humidified gases were supplied to the *in situ* XAFS cell heated at 353 K, resulting in ~ 93% relative humidity (RH). The MEAs in the XAFS cell were conditioned by 150 aging cycles with a sequence of step-wise galvanostatic current steps every 6 s from open circuit voltage (OCV) to a potential near 0.3 V_{RHE} in H_2 (anode) and air (cathode) operating atmospheres. The samples conditioned by the aging treatment are denoted as activated samples hereinafter. The cathode degradation was carried out by accelerated durability test (ADT) cycles with a triangular wave between 1.0 and 1.5 V_{RHE} at 0.5 V s^{-1} in H_2 (anode) and N_2 (cathode) operating atmospheres. Cyclic voltammograms (CVs) and I-V loads under were measured after the aging treatment and ADT cycles. The CV measurements in *in situ* PEFC conditions were conducted between 0.05 and 0.9 V_{RHE} at 20 mV s^{-1} in H_2 (anode) and N_2 (cathode) operating atmospheres. The electrochemical surface areas (ECSAs) of the cathode catalysts in MEAs at 353K were calculated by charge density of H_2 adsorption on a Pt surface (210 μC/$cm_{\text{-Pt}}^2$) in the H_2 underpotential deposition region (0.05 V– ca. 0.4 V of the onset of the double-layer region). [36,37]

2.2. *In situ/operando* time-resolved XAFS measurements and XAFS data analysis. The series of *in situ/operando* time-resolved XAFS spectra at Pt L_{III}-edge for Pt/KB, Pt/AB and Pt/MWCNT cathode

catalysts in PEFC MEAs under transient potential operations (anode: H_2; cathode: N_2 or air; 353 K; ~93% relative humidity) were measured in a transmission mode at BL36XU station in SPring-8 using ion chambers (I_0: Ar 15%/N_2 85%; I_t: N_2 100%) for incident and transmitted X-rays, respectively and using a Si(111) double-crystal monochromator as shown in ESI Figure S1.[38] In ESI Figure S1 the experimental setup for *in situ* time-resolved XAFS measurements by a home-made XAFS cell, while measuring the current/charge of PEFC during the potential operating processes, is illustrated.[35-38] The BL36XU beamline with several XAFS systems for characterization of fuel cells with the highest-level performances was constructed by our group under a NEDO program.[49] The cell voltage was changed from the open-circuit voltage (OCV) to 0.4 V_{RHE}, where the voltage was kept for 300 s, followed by the rapid voltage jump from 0.4 V_{RHE} to1.4 V_{RHE} (at time=zero for the transient voltage up process), and this voltage was kept for 300 s, and then reversely, the cell voltage was jumped rapidly from 1.4 V_{RHE} to 0.4 V_{RHE} (at time=zero for the transient voltage down process) as shown in ESI Figure S2. The transient responses of the MEA cathode catalysts against the voltage cycling operations were measured by QXAFS at a time resolution of 100 ms for 30 s from 10 s before each voltage jump (ESI Figure S2).

QXANES and QEXAFS spectra were analyzed in the similar way to the previous reports,[7,38,46-48] using the Larch code containing the IFEFFIT Package ver.2 (Athena and Artemis).[27,50] The white line peaks of normalized QXANES spectra were analyzed by curve fitting with a Lorentzian function and an arctangent function. Error ranges of the QXANES curve fitting were estimated as 95% confidence intervals. Background subtraction in the QEXAFS analysis was performed using Autobk.[51] The Victoreen function was employed for the background subtraction and the spline smoothing method with Cook and Sayers criteria was used as the μ_0 method. The extracted k^2-weighted EXAFS oscillations were Fourier-transformed to R-space over k = 30–110 nm^{-1}, and the curve fittings were performed in the R-space (0.13–0.32 nm). The effect of k-range on the EXAFS analysis results is described in ESI page S18. The fitting parameters for each shell were coordination number (CN), interatomic distance (R), Debye-Waller factor (σ^2), and correction-of-edge energy (ΔE_0). The phase shifts and amplitude functions for Pt-Pt and Pt-O were calculated from the FEFF 8.4 code using structural parameters obtained from the crystal structures of Pt and PtO.[52] The amplitude reduction factor (S_0^2) for Pt-Pt bonds in this study was estimated to be 0.836 by analyzing Pt foil. Error ranges of the curve-fitting analysis of EXAFS Fourier transforms were based on the definition of the Larch code.[50] The quality of the observed 100 ms time-resolved QEXAFS data was good enough for achieving the curve-fitting analysis, but when the error ranges of 100 ms-resolved QXAFS analysis

were large and scattered, three 100 ms-resolved QXAFS spectra (100 ms x 3) were merged for the QXAFS analysis.

2.3. Rate constant decision. The white line peak intensity (area) of the Pt L_{III}-edge QXANES and the coordination number (CN) and interatomic distance (R) of Pt-Pt and Pt-O, respectively and the current/charge variation of PEFC MEA recorded on the electrochemical P/G stat were plotted against time (*t*) in the transient response processes under the potential jump of 0.4 V_{RHE} →1.4 V_{RHE} and 1.4 V_{RHE} →0.4 V_{RHE}. The rate constants for the electrochemical and surface chemical reaction processes determined from the time change in the above parameters were estimated by data fitting using an exponential function for the QXAFS analysis data or a linear combination of two exponential functions for the current/charge variation, taking into account the error weighting given by the inverse of the error. The data fitting with one or two exponential functions for the change of each parameter against time (t) was performed for the period of 0–20 s after the voltage was jumped (0.4 V_{RHE} → 1.4 V_{RHE} and 1.4 V_{RHE} → 0.4 V_{RHE}). The fitting equation by an exponential function is typically given by eq. (1), where *u* and *d* denote potential up and down processes, respectively, *y* is an experimentally determined constant, and $k_{1\alpha}$ is a rate constant. It is to be noted that the analysis of QXAFS data by exponential functions to determine the first-order rate constants is independent of Pt quantity and Pt utilization in MEAs and reflects the dynamic changes of the Pt valence and coordination structure in the transient response processes against the potential operations.

$$\begin{aligned} f_\alpha(t) &= \begin{cases} y_{0\alpha} & t < 0 \\ y_{1\alpha} + A_{1\alpha}\exp(-k_{1\alpha}t) & t \geq 0 \end{cases} \quad (\alpha = u, d) \\ A_{1\alpha} &= y_{0\alpha} - y_{1\alpha} \end{aligned} \tag{1}$$

3. RESULTS AND DISCUSSION

3.1. Mass activities and surface specific activities of Pt/KB, Pt/AB, and Pt/MWCNT in PEFC. By increasing triangular 1.0-1.5 V_{RHE} ADT cycles the initial maximum power densities for Pt/KB, Pt/AB, and Pt/MWCNT in PEFC MEAs decreased to about 55-60% of each initial value after 1000 ADT cycles for Pt/KB and 5000 ADT cycles for Pt/AB and Pt/MWCNT. Hence, in this study the activated samples after the conditioning (aging) treatment and the degraded samples after the ADT cycles were compared to each other to explore the key structural kinetics for the ORR activity and

durability of the three Pt/C cathode catalysts and to understand the carbon effects on the Pt/C electrocatalysis in PEFC.

Mass activities (MA: current per mg-Pt) and surface specific activities (SA: current per cm^2-Pt) for the Pt/KB, Pt/AB and Pt/MWCNT cathode catalysts in MEAs were calculated from the kinetic activities evaluated by semi-logarithmic plots of I-V polarization curves using the current densities at 0.9 V_{RHE} as shown in ESI Figures S3-S5, at which voltage the mass transport losses can be neglected.[53,54] The MA and SA values are listed in Table 1, where electrochemical surface areas (ECSAs) estimated from the hydrogen desorption and adsorption areas in CVs are also shown.[35-38] The results indicate a significant effect of the kind of carbon supports on the activity and durability of the MEAs. The XRD patterns and TEM images revealed that the Pt nanoparticles of the three Pt/C cathode catalysts possessed similar dimensions around 2.9 nm ± 0.5 nm on average as reported in our previous study.[37] It is known that the ORR activity of Pt/C electrocatalysts changes with Pt particle size.[35,38] Thus, we can avoid the particle size effect from the present discussion on the structural kinetics of elementary steps for the ORR to uncover the key issue and origin of the difference in the cathode activity among the Pt/KB, Pt/AB and Pt/MWCNT catalysts (MA and SA: Pt/KB > Pt/AB > Pt/MWCNT (Table 1)). After the ADT cycles for Pt/KB, Pt/AB and Pt/MWCNT, the Pt nanoparticle

Table 1. Mass activities and surface specific activities of Pt/KB, Pt/AB and Pt/MWCNT in MEAs, and their relative activities normalized to the aging Pt/MWCNT and to each aging catalyst

Measured values

	Pt/KB		Pt/AB		Pt/MWCNT	
	activated	ADT1000	activated	ADT5000	activated	ADT5000
mass activity / A mg^{-1}_{Pt}	0.02	0.0061	0.0087	5.65E-04	0.0038	0.0053
specific activity / μA cm^{-2}_{Pt}	39.7	24.9	24.3	3.1	14.8	38.2
ECSA/ m^2 g^{-1}_{Pt}	48.8	25.3	40.9	18.3	27.5	14.6

Relative values, normalized to those of the activated Pt/MWCNT

	Pt/KB		Pt/AB		Pt/MWCNT	
	activated	ADT1000	activated	ADT5000	activated	ADT5000
mass activity	5.26	1.61	2.29	0.15	1.00	1.39
specific activity	2.68	1.68	1.64	0.21	1.00	2.58

Relative values, normalized to each activated catalyst, respectively

	Pt/KB		Pt/AB		Pt/MWCNT	
	activated	ADT1000	activated	ADT5000	activated	ADT5000
mass activity	1.00	0.31	1.00	0.06	1.00	1.39
specific activity	1.00	0.63	1.00	0.13	1.00	2.58

size increased to 6.5 nm ±1.5 nm for all cathode catalysts, and hence we can compare the time-resolved QXAFS data for the degraded Pt/C samples with the similar Pt nanoparticle sizes to discuss on the key structural kinetics most relevant to the durability of MEA Pt/C cathode catalysts.

3.2. *In situ* time-resolved Pt L_{III}-edge QXAFS analysis of the Pt/KB, Pt/AB and Pt/MWCNT.

3.2.1. Potential-dependent surface structures of Pt nanoparticles at the cathodes. Figure 1 and Figure 2 show the series of *in situ* time-resolved Pt L_{III}-edge QXANES spectra (every 100 ms) and QEXAFS Fourier transforms (every 300 ms (100 ms x3, merged)), respectively, for Pt/AB in PEFC MEAs as a typical cathode catalyst after the conditioning (activating) and ADT cycles in the transient potential operation processes (0.4 V_{RHE} → 1.4 V_{RHE} and 1.4 V_{RHE}→ 0.4 V_{RHE}) under H_2(anode)-N_2(cathode). The series of *in situ* time-resolved Pt L_{III}-edge QXANES spectra and QEXAFS Fourier transforms for the three MEA cathode catalysts, Pt/KB, Pt/AB and Pt/MWCNT, under both H_2(anode)-N_2(cathode) and H_2(anode)-air(cathode) are shown in ESI Figures S6-S8 and ESI Figures S9-S11, respectively. The white line intensities (peak areas) in the QXANES spectra for Pt/KB, Pt/AB and Pt/MWCNT after the conditioning (activating) and ADT cycles, which reflect a Pt valence of the Pt/C cathodes,[35-38] were estimated by curve fitting with a Lorentzian function and an arctangent function as

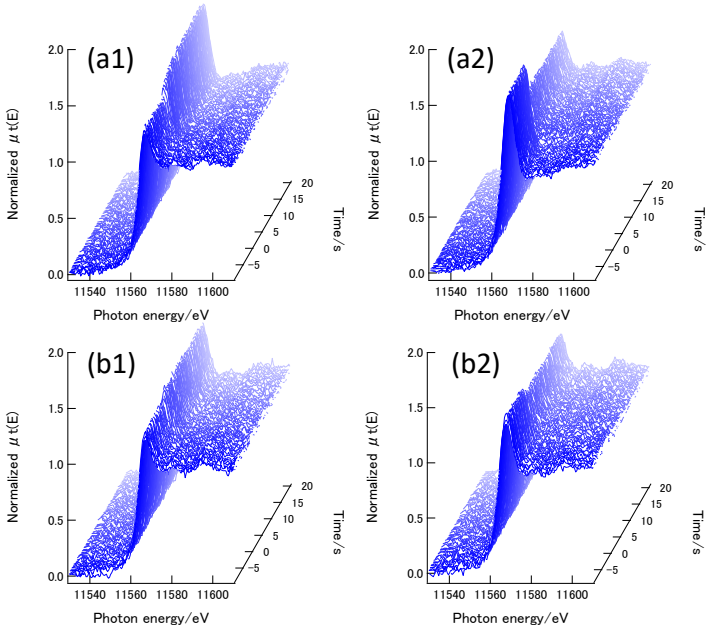

Figure 1. The series of *in-situ* time-resolved Pt L_{III}-edge QXANES spectra (every 100 ms) for Pt/AB after the conditioning (activating) (a) and ADT 5000 cycles (b) in the potential jump processes under H_2(anode)-N_2(cathode). (1) 0.4 V_{RHE} → 1.4 V_{RHE} and (2) 1.4 V_{RHE} → 0.4 V_{RHE}.

shown in ESI Figure S12, where the QXANES spectra and curve fittings at 0.4 V_{RHE} and 1.4 V_{RHE} are typically presented. Oxidation of Pt is clear at 1.4 V_{RHE} for all three catalysts, as indicated by the increase in the Pt L_{III}-edge QXANES white line intensity compared to that in the metallic state at 0.4 V_{RHE}.

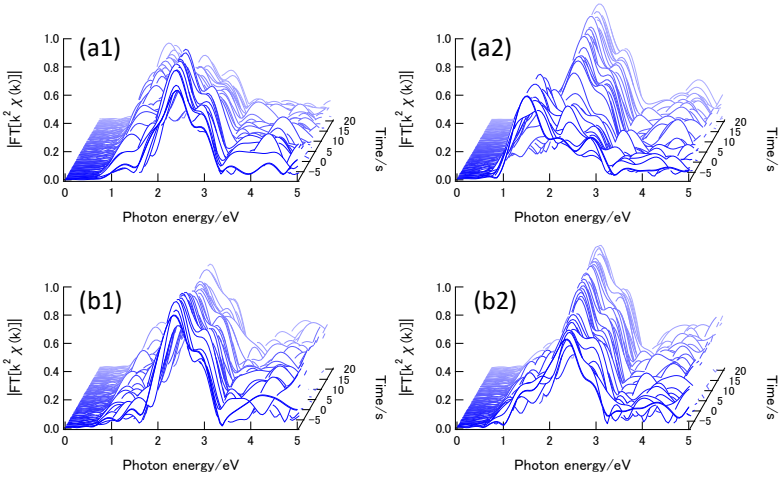

Figure 2. The series of Fourier transforms of *in-situ* time-resolved Pt L_{III}-edge QEXAFS spectra (every 300 ms) for Pt/AB after the conditioning (activating) (a) and ADT 5000 cycles (b) in the potential jump processes under H_2(anode)-N_2(cathode). (1) 0.4 V_{RHE} → 1.4 V_{RHE} and (2) 1.4 V_{RHE} → 0.4 V_{RHE}.

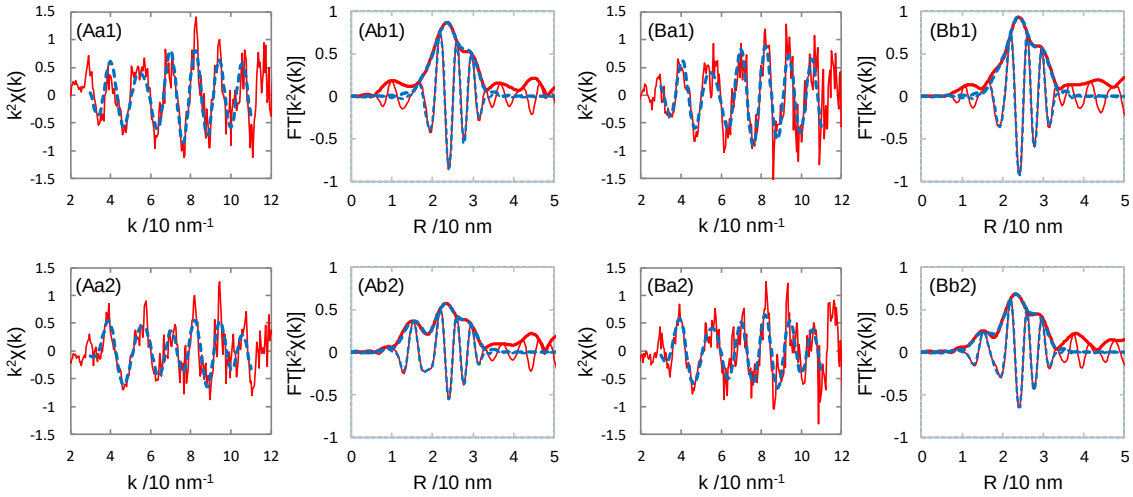

Figure 3. k^2-weighted Pt L_{III}-edge QEXAFS oscillations (a) and their associated Fourier transforms (b) (100 ms x3, merged) for Pt/MWCNT after the conditioning (activating) (A) and ADT 5000 cycles (B) at 0.4 V_{RHE} (1) and 1.4 V_{RHE} (2) under H_2 (anode) -N_2 (cathode) flow. Fitting curves: dashed; Fitting ranges: 30 – 110 nm^{-1} for Δk and 0.13 – 0.32 nm for ΔR.

Figure 3 and ESI Figures S13-15 show the k^2-weighted QEXAFS oscillations and their associated Fourier transforms (every 300 ms (100 ms x3, merged)) for the Pt/KB, Pt/AB and Pt/MWCNT cathode catalysts in activated and ADT-degraded PEFC MEAs typically under the H_2 (anode) -N_2 (cathode) operating conditions at 0.4 V_{RHE} and 1.4 V_{RHE}. The structural parameters of the local coordination of the Pt/KB, Pt/AB and Pt/MWCNT in MEAs were determined by the curve fitting analysis of the Pt

Table 2. Curve-fitting results of the k^2-weighted QEXAFS data for Pt/KB, Pt/AB and Pt/MWCNT in MEAs after the conditioning (activating) and ADT cycles in H_2-N_2

(1) Pt/KB (activated)

Potential/V_{RHF}	Bond	CN	σ^2 / 10^{-4}nm^2	E_0 / eV	R / nm	R_f / %
0.4	Pt-Pt	10.0 ± 0.7	0.538 ± 0.067	5.1 ± 0.9	0.275 ± 0.001	0.5
1.4	Pt-Pt	5.1 ± 1.7	0.693 ± 0.442	5.3 ± 1.8	0.274 ± 0.001	0.8
	Pt-O	2.2 ± 0.5	0.463 ± 0.188		0.202 ± 0.001	

(2) Pt/KB (ADT 1000)

Potential/V_{RHF}	Bond	CN	σ^2 / 10^{-4}nm^2	E_0 / eV	R / nm	R_f / %
0.4	Pt-Pt	11.0 ± 1.4	0.746 ± 0.110	5.3 ± 1.3	0.275 ± 0.001	1.2
1.4	Pt-Pt	6.5 ± 1.0	0.602 ± 0.121	4.8 ± 1.1	0.276 ± 0.001	0.4
	Pt-O	1.3 ± 0.4	0.646 ± 0.266		0.200 ± 0.001	

(3) Pt/AB (activated)

Potential/V_{RHF}	Bond	CN	σ^2 / 10^{-4}nm^2	E_0 / eV	R / nm	R_f / %
0.4	Pt-Pt	10.4 ± 1.8	0.678 ± 0.158	4.5 ± 2.0	0.275 ± 0.001	2.4
1.4	Pt-Pt	6.1 ± 1.0	0.799 ± 0.156	4.5 ± 1.1	0.275 ± 0.001	0.3
	Pt-O	2.1 ± 0.31	0.648 ± 0.175		0.201 ± 0.001	

(4) Pt/AB (ADT 5000)

Potential/V_{RHF}	Bond	CN	σ^2 / 10^{-4}nm^2	E_0 / eV	R / nm	R_f / %
0.4	Pt-Pt	10.3 ± 0.9	0.648 ± 0.066	3.9 ± 0.8	0.276 ± 0.001	0.4
1.4	Pt-Pt	8.8 ± 1.9	0.665 ± 0.177	3.4 ± 1.7	0.275 ± 0.001	1.0
	Pt-O	0.7 ± 0.6	0.538 ± 0.759		0.198 ± 0.003	

(5) Pt/MWCNT (activated)

Potential/V_{RHF}	Bond	CN	σ^2 / 10^{-4}nm^2	E_0 / eV	R / nm	R_f / %
0.4	Pt-Pt	11.0 ± 0.7	0.635 ± 0.055	4.5 ± 0.7	0.275 ± 0.001	0.3
1.4	Pt-Pt	8.5 ± 0.6	0.546 ± 0.068	1.2 ± 0.7	0.273 ± 0.001	0.2
	Pt-O	0.8 ± 0.1	0.015 ± 0.146		0.196 ± 0.001	

(6) Pt/MWCNT (ADT 5000)

Potential/V_{RHF}	Bond	CN	σ^2 / 10^{-4}nm^2	E_0 / eV	R / nm	R_f / %
0.4	Pt-Pt	11.0 ± 0.8	0.513 ± 0.063	3.6 ± 0.9	0.274 ± 0.001	0.4
1.4	Pt-Pt	8.4 ± 1.2	0.476 ± 0.105	2.7 ± 1.2	0.275 ± 0.001	0.4
	Pt-O	0.9 ± 0.4	0.397 ± 0.527		0.199 ± 0.002	

L_{III}-edge QEXAFS Fourier transforms (Figure 3 and ESI Figures S13-15). The determined structural parameters are listed in Table 2.

For the cathode catalysts at 0.4 V_{RHE} in the activated samples only Pt-Pt bonds at 0.275 ±0.001 nm were observed, indicating the metallic state of Pt nanoparticles on KB, AB and MWCNT supports in the activated samples. The coordination numbers (CN) of Pt-Pt were 10.0 ± 0.7 for Pt/KB, 10.4 ±1.8 for Pt/AB, and 11.0 ±0.7 for Pt/MWCNT, respectively as shown in Table 2. The observed CN(Pt-Pt) values well coincide with 10.8 expected from the Pt nanoparticle size of 2.9 nm ±0.5 nm.[38] The Pt nanoparticles with 2.9 nm dimension are regarded to constitute approximately 6 Pt layers (the sixth, fifth, fourth, third, second, and first layers and a central atom), assuming sphere structures with the fcc arrangement (d_{111} (interplanar spacing) ~0.226 nm), and hence the CN(Pt-Pt) is estimated to be 10.8 by the equation, $CN(Pt\text{-}Pt)=(12*(1^2+2^2+3^2+4^2+5^2)+9*6^2)/ (1^2+2^2+3^2+4^2+5^2+6^2)=10.8$, where 12 is the CN of Pt atoms in fcc Pt bulk(1^{st}-5^{th} Pt layer) and 9 is the CN of Pt atoms at the outermost surface (6^{th} Pt layer).[35,37,38] Here, we follow the previous estimation approach to the average CNs. Accurate CNs for crystalline (cubo-octahedral, cubic, etc.) metal nanoparticles have been discussed in detail.[55-57] It is, in general, hard to detect the interface bonding like Pt-C between Pt nanoparticles and carbon surfaces due to mismatch of the lattice parameters and disordered/amorphous carbon surfaces involving different Pt-C interatomic distances and diminishing Pt-C contribution.

At 1.4 V_{RHE}, the Fourier transforms of the QEXAFS data for the activated samples were fitted with two shells of Pt-Pt at 0.273-0.274 ±0.003 nm and Pt-O at 0.196-0.202 ±0.003 nm (Table 2), indicating the oxidation of the Pt catalyst surface as reported previously for Pt/KB, Pt_3Co/KB, Pt_3Ni/KB, SnO_2/Pt/KB and SnO_2/Pt_3Co/KB.[6,7,35-38,45-48] The CN(Pt-Pt) and CN(Pt-O) for Pt/KB, Pt/AB and Pt/MWCNT were determined to be 5.1 ±1.7 and 2.2 ± 0.5, 6.0 ±1.0 and 2.1 ±0.31, and 8.5 ±0.6 and 0.8 ±0.1, respectively (Table 2). From the CN(Pt-Pt) and CN(Pt-O) we estimated the surface structures of Pt nanoparticles on KB, AB and MWCNT at 1.4 V_{RHE} in a similar way to that described in our previous study.[35,38] When adsorbed oxygen atoms are located only at the Pt surface, almost no CN(Pt-Pt) should change, but actually the CN(Pt-Pt) decreased drastically from 10.8 to 5.1-8.5, which indicates the existence of both surface oxygen and subsurface oxygen, forming a surface $Pt^{2+}O$ layer. [6,7,35-38,45-548] The aspect is compatible with the previous reports.[58,59] The observed Pt-O bond distances of 0.196-0.202 ±0.003 nm (Table 2) are similar to 0.200 nm for tetragonal PtO phase as shown in Figure 4. By assuming a full coverage of tetragonal PtO phase at the Pt nanoparticle surface (Figure 4 (b)), the CN(Pt-Pt) and CN(Pt-O) values are estimated to be 6.4 and 2.1, respectively by the equations,

CN(Pt-Pt)= $12*(1^2+2^2+3^2+4^2)*x/(1^2+2^2+3^2+4^2+5^2+6^2)+9*5^2*x/(1^2+2^2+3^2+4^2+5^2+6^2)$=6.4 and CN(Pt-O)= $(6^2*x*4+5^2*x*2)/(1^2+2^2+3^2+4^2+5^2+6^2)$ =2.1, where *x* is 1 (at full coverage). These values reproduce the observed CN values for Pt/KB and Pt/AB (Table 2). However, there may exist some distortion of the second Pt layer by the existence of the subsurface oxygen atoms, resulting in the smaller CN(Pt-Pt) values a little than the calculated ones. As for the Pt/MWCNT, the observed CN(Pt-Pt) of 8.5 and the observed CN(Pt-O) of 0.8 were larger than 6.4 and smaller than 2.1, respectively expected from the full coverage of PtO phase, indicating a partial coverage of PtO phase. When the PtO coverage is half (x=1/2) at the surface (Figure 4 (c)), the estimated CN(Pt-Pt) and CN(Pt-O) are 8.6 and 1.07, respectively, which agree with the observed values 8.5 ±0.6 and 0.8 ±0.1, respectively. The potential dependent surface structures at 0.4 V_{RHE} and 1.4 V_{RHE} for Pt/KB, Pt/AB and Pt/MWCNT are illustrated in (a) and (b) and (a) and (c) of Figure 4, respectively. The observed XANES spectra were well reproduced by a linear combination of Pt foil and $Pt^{2+}O$ similar to the previous work.[35]

The structural parameters under H_2 (anode) - Air (cathode) are summarized in ESI Table S1. Besides Pt-Pt contribution, Pt-O contribution (CNs of Pt-O: 0.2 -0.5) was also observed with Pt/KB, Pt/AB and Pt/MWCNT at 0.4 V_{RHE}. The CNs of Pt-Pt for the three cathode catalysts at the ORR steady

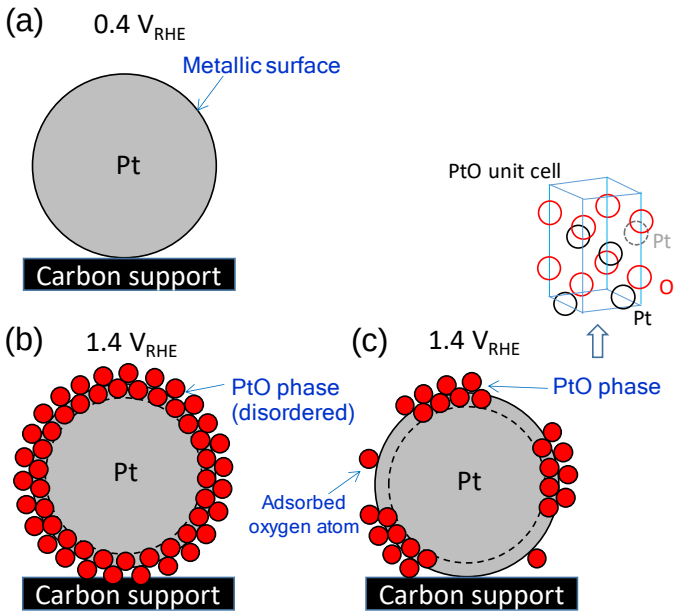

Figure 4. Potential-dependent surface structures of Pt nanoparticles in Pt/KB, Pt/AB and Pt/MWCNT cathodes at 0.4 V_{RHE} and 1.4 V_{RHE}. (a) Pt/KB, Pt/AB and Pt/MWCNT at 0.4 V_{RHE}. (b) Pt/KB and Pt/AB at 1.4 V_{RHE}. (c) Pt/MWCNT at 1.4 V_{RHE}. A tetragonal PtO unit cell with a dashed gray circle in the adjacent cell is also shown; Pt-O: 0.200 nm, CN(Pt-O): 4.

state under H_2 (anode) - Air (cathode) were almost the same as the corresponding CNs under H_2 (anode) - N_2 (cathode) at 0.4 V_{RHE}, which means that the adsorbed oxygen species are located only at the Pt surface under H_2 (anode) - Air (cathode) flow. At 1.4 V_{RHE} the CN(Pt-Pt) and CN(Pt-O) for Pt/KB, Pt/AB and Pt/MWCNT were estimated to be 5.0 ± 1.2 and 1.7 ± 0.3, 5.4 ± 1.0 and 1.5 ± 0.3, and 8.5 ± 0.7 and 0.9 ± 0.2, respectively by the QEXAFS curve fitting analysis. These values are almost the same as those for the corresponding catalysts under H_2 (anode) - N_2 (cathode), respectively, indicating the similar surface structures and electronic state of Pt nanoparticles under both cathode gas conditions at 1.4 V_{RHE}. In air the ORR at the cathode proceeds steadily, and the QXAFS spectra reflect the local coordination and electronic state of the Pt catalysts under the steady-state ORR conditions.[50,51]

The Pt nanoparticles in Pt/KB, Pt/AB and Pt/MWCNT grew to 6.5 nm ±1.5 nm (~14 Pt layers) after the ADT cycles. Similar to the cases of activated samples, the CN(Pt-Pt) at 0.4 V_{RHE} was estimated to be 11.4 (ESI), which reproduces the observed CN(Pt-Pt) values under H_2 (anode) - N_2 (cathode) (the values under H_2 (anode) - Air (cathode) in bracket); 11.0 ±1.4 (10.7 ±1.2), 10.3 ±0.9 (10.3 ±1.0) and 11.0 ± 0.8 (10.1 ± 1.7), respectively for Pt/KB (ADT 1000), Pt/AB (ADT 5000) and Pt/MWCNT (ADT 5000) (Table 2 and Table S1). At 1.4 V_{RHE}, the CN(Pt-Pt) and CN(Pt-O) were estimated to be 9.4 and 1.1, respectively (ESI), which also totally reproduce the observed CN(Pt-Pt) and CN(Pt-O) values under H_2 (anode) - N_2 (cathode) (under H_2 (anode) - Air (cathode) in bracket); 6.5 ±1.0 (7.2 ±1.4) and 1.3 ±0.4 (1.2 ±0.4), 8.8 ±1.9 (9.5 ±1.4) and 0.7 ±0.6 (0.7 ±0.4), and 8.4 ±1.2 (8.1 ±1.4) and 0.9 ±0.4 (0.9 ±0.6), respectively for Pt/KB (ADT 1000), Pt/AB (ADT 5000) and Pt/MWCNT (ADT 5000). The smaller CN(Pt-Pt) may indicate some distortion at the13th Pt layer underneath the PtO phase. These results reveal the similar surface structures of Pt nanoparticles under both cathode gas conditions at 0.4 V_{RHE} and 1.4 V_{RHE} (Figure 4) except the partial presence of surface oxygen species at 0.4 V_{RHE} under H_2 (anode) - Air (cathode).

3.2.2. *In situ* time-resolved Pt L_{III}-edge QXAFS analysis under transient potential operations. The ORR activity of the cathode catalysts in automotive PEFCs under the practical potential changing processes may be related to the structural kinetics of elementary reaction steps (the rate constants (k and k') of structural and electronic transformations) at the cathode Pt surface in the transient potential operations, involving charging ($k_{valence}$)/discharging ($k'_{valence}$) of cathode Pt nanoparticles, Pt-O bond formation (k_{Pt-O})/dissociation (k'_{Pt-O}) and Pt-Pt bond dissociation (k_{Pt-Pt})/rebonding (k'_{Pt-Pt}), which can

be determined by *in situ* time-resolved QXAFS, while measuring the electrochemical current/charge simultaneously.[7,27,38,45-48]

The temporal variations in the electronic and structural parameters of the Pt/KB, Pt/AB and Pt/MWCNT cathode catalysts in MEAs during the transient voltage cycling processes (0.4 V_{RHE} → 1.4 V_{RHE} → 0.4 V_{RHE}) under H_2 (anode) - N_2 (cathode) and H_2 (anode) - Air (cathode) were investigated by *in situ* time-resolved Pt L_{III}-edge QXAFS. The series of both QXANES spectra and Fourier transforms of k^2-weighted QEXAFS oscillations at Pt L_{III}-edge for the Pt/KB, Pt/AB and Pt/MWCNT cathodes after the conditioning (activating) and ADT cycles under the transient potential operation in H_2 (anode) - N_2 (cathode) and H_2 (anode) - Air (cathode) were obtained as shown in Figure 1, Figure 2 and ESI Figures S6-S8, and ESI Figure S9-S11, respectively. In the voltage change from 0.4 V_{RHE} to 1.4 V_{RHE}, the white line peak intensity (Pt valence) increased with time, and in the reverse transient process from 1.4 V_{RHE} to 0.4 V_{RHE} the white line peak intensity (Pt valence) decreased with time. The curve-fitting analysis of the series of QEXAFS Fourier transforms revealed the formation of Pt-O bonds (increase of CN(Pt-O)) and the dissociation of Pt-Pt bonds (decrease of CN(Pt-Pt)) in the transient process from 0.4 V_{RHE} to 1.4 V_{RHE}, and reversely the dissociation of the formed Pt-O bonds (decrease of CN(Pt-O)) and the reformation of the dissociated Pt-Pt bonds (increase of CN(Pt-Pt)) proceeded in the transient process from 1.4 V_{RHE} to 0.4 V_{RHE}.

The transient responses of the white line peak intensity (peak areas) determined by the time-resolved QXANES analysis (every 100 ms or 300 ms (100 ms x3, merged)) and the CNs of Pt-Pt and Pt-O bonds determined by the time-resolved QEXAFS analysis (every 100 ms or 300 ms (100 ms x3, merged)) for the Pt/KB, Pt/AB and Pt/MWCNT cathodes in MEAs after the conditioning (activating) and ADT cycles were plotted against the time before and after the potential operation in Figures 5, 6 and 7, respectively, where the transient potential steps 0.4 V_{RHE} → 1.4 V_{RHE} and 1.4 V_{RHE} → 0.4 V_{RHE} were operated at time zero. The current in the cell recorded on the potentiostat/galvanostat (P/G stat) system changed immediately after the potential change, whose results are also shown in Figures 5, 6 and 7, respectively. The actual electrochemical reactions in the cell due to the voltage change were estimated by subtracting the background oxidation in the cell.[46] The transient response profiles in the white line peak area (proportional to Pt valence), CN(Pt-Pt), CN(Pt-O), and cell currents for the Pt/KB, Pt/AB and Pt/MWCNT catalysts were successfully fitted with an exponential function (eq.1) for the electronic and structural parameter profiles and with two exponential functions for the current profiles as shown by blue dashed curves in Figures 5, 6 and 7, respectively. The coefficient $k_{1\alpha}$ in the

exponential function (eq. 1) corresponds to the rate constant of the chemical reaction event at the Pt cathode surface. The determined rate constants are influenced not by the Pt quantity and Pt utilization in MEAs but by the working state of active Pt nanoparticles. This may be an advantage of the XAFS analysis of active catalyst itself over macroscopic electrochemical analysis. The estimated rate constants (k and k' for the potential up and down, respectively) for the electrochemical reactions (measured every 20 ms) and the electronic (Pt valence) and structural (CN(Pt-Pt) and CN(Pt-O)) changes (measured every 100 ms) at the Pt/KB, Pt/AB and Pt/MWCNT in MEAs after the conditioning (activating) and ADT cycles in the potential operations under H_2(anode)-N_2(cathode) with a relative humidity of ~ 93% at 353 K (cell temp.) are listed in Table 3, and the 10 elementary reaction steps and their rate constants for the three activated catalysts are also summarized in Figure 8 (the data after ADT cycles are not shown to avoid crowdedness). The Pt valence change, the CN(Pt-Pt) change and the CN(Pt-O) change were much slower than the current/charge response (the faster exponential coefficient). The similar aspect has been indicated with the rate constants for the surface reaction steps on the samples, Pt/KB, Pd@Pt(1 ML)/KB, Pd@Pt(2 ML)/KB, Pt_3Co/KB and Pt_3Ni/KB.[38,45-48] The slower surface Pt oxide formation than the electrochemical current/charge response during square-

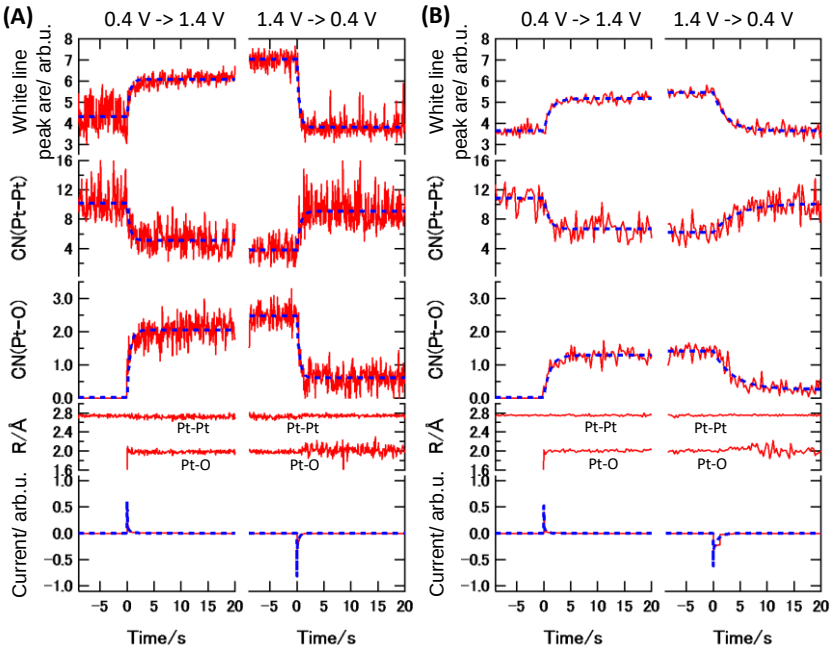

Figure 5. Transient response curves of the white line intensity, CN(Pt-Pt), CN(Pt-O), R(Pt-Pt), R(Pt-O), and current for Pt/KB after the conditioning (activating) (A) and ADT 1000 cycles (B) in the voltage up (0.4 V_{RHE} -→ 1.4 V_{RHE}) and down (1.4 V_{RHE} -→ 0.4 V_{RHE}) cycles under H_2(anode)-N_2(cathode); Cell temp.: 353 K, Relative humidity: ~ 93%. (A) every 100 ms; (B) every 300 ms.

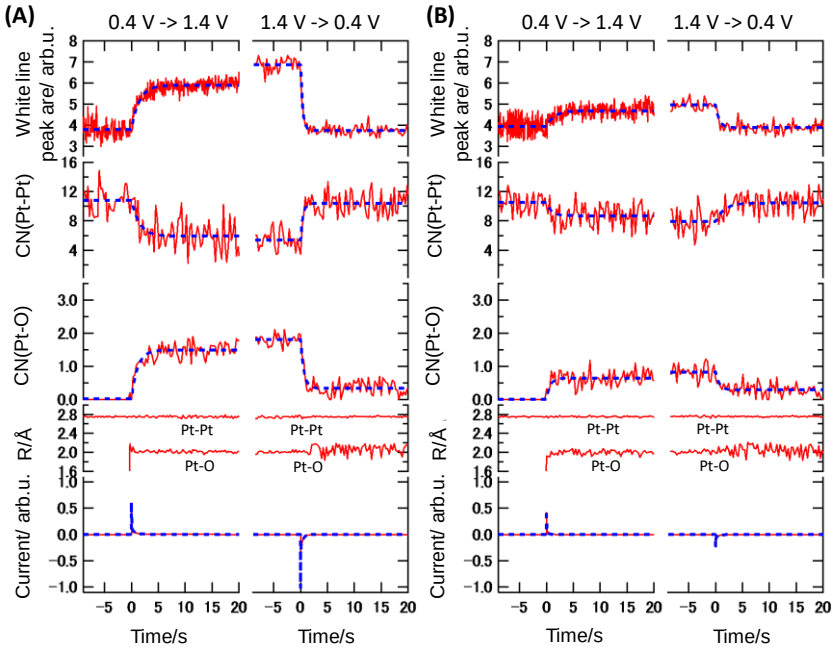

Figure 6. Transient response curves of the white line intensity, CN(Pt-Pt), CN(Pt-O), R(Pt-Pt), R(Pt-O), and current for Pt/AB after the conditioning (activating) (A) and ADT 5000 cycles (B) in the voltage up (0.4 V_{RHE} -→ 1.4 V_{RHE}) and down (1.4 V_{RHE} -→ 0.4 V_{RHE}) cycles under H_2(anode)-N_2(cathode); Cell temp.: 353 K, Relative humidity: ~ 93%. Time resolution: see Table 3.

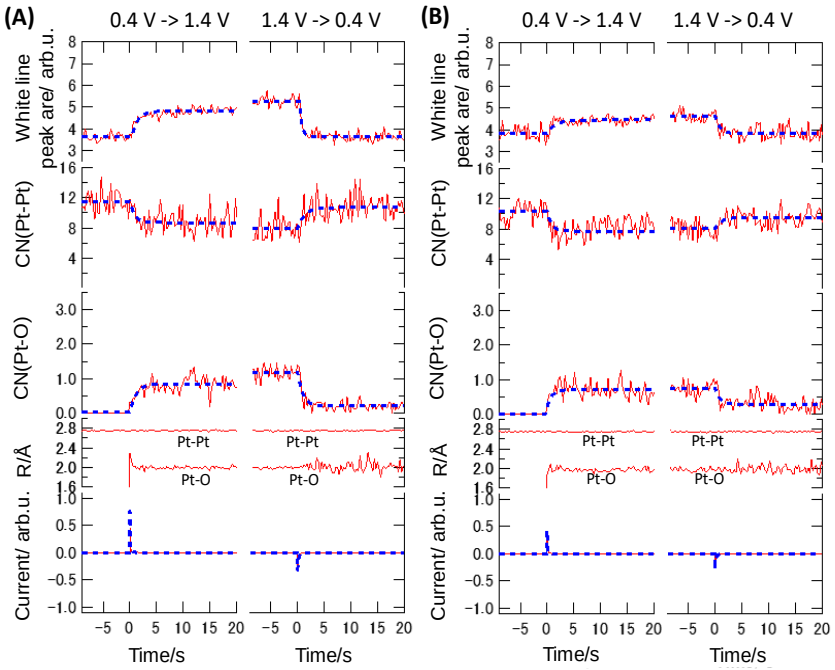

Figure 7. Transient response curves of the white line intensity, CN(Pt-Pt), CN(Pt-O), R(Pt-Pt), R(Pt-O), and current for Pt/MWCNT after the conditioning (activating) (A) and ADT 5000 cycles (B) in the voltage up (0.4 V_{RHE} -→ 1.4 V_{RHE}) and down (1.4 V_{RHE} -→ 0.4 V_{RHE}) cycles under H_2(anode)-N_2(cathode); Cell temp.: 353 K, Relative humidity: ~ 93%. Time resolution: see Table 3.

Table 3. Rate constants (k and k') for the electrochemical reactions and the electronic (Pt valence) and structural (CN(Pt-Pt) and CN(Pt-O)) changes at Pt/KB, Pt/AB and Pt/MWCNT cathodes in MEAs after the conditioning (activating) and ADT cycles in the potential operations under H_2(anode)-N_2(cathode); Cell temp.: 353 K, Relative humidity: ~ 93%

	Pt/KB		Pt/AB		Pt/MWCNT	
	Activated	ADT 1000	Activated	ADT 5000	Activated	ADT 5000
$k_{valence}$ (1) and $k'_{valence}$ (2) in s^{-1}						
(1) 0.4 V -> 1.4 V	1.92± 0.153[a]	0.81 ± 0.109[b]	0.692 ± 0.0737[a]	0.672 ± 0.217[a]	0.853 ± 0.143[b]	0.647 ± 0.287[b]
(2) 1.4 V -> 0.4 V	2.17 ± 0.287[a]	0.41 ± 0.0375[b]	2.76 ± 0.364[b]	1.49 ± 0.461[b]	2.10 ± 0.373[b]	1.11 ± 0.447[b]
k_{Pt-Pt} (1) and k'_{Pt-Pt} (2) in s^{-1}						
(1) 0.4 V -> 1.4 V	1.87 ± 0.608[a]	1.06 ± 0.407[b]	0.664 ± 0.231[b]	0.739 ± 0.629[b]	1.12 ± 0.692[b]	1.02 ± 0.721[b]
(2) 1.4 V -> 0.4 V	1.59 ± 0.48[a]	0.236 ± 0.0685[b]	2.41 ± 1.43[b]	0.85 ± 0.352[b]	0.748 ± 0.395[b]	0.829 ± 0.525[b]
k_{Pt-O} (1) and k'_{Pt-O} (2) in s^{-1}						
(1) 0.4 V -> 1.4 V	1.82 ± 0.236[a]	0.852 ± 0.122[b]	0.879 ± 0.122[b]	1.00 ± 0.501[b]	0.842 ± 0.177[b]	1.16 ± 0.512[b]
(2) 1.4 V -> 0.4 V	2.05 ± 0.304[a]	0.273 ± 0.0325[b]	1.68 ± 0.309[b]	1.47 ± 0.689[b]	1.03 ± 0.199[b]	1.18 ± 0.975[b]
k_e (1) and k'_e (2) in s^{-1}						
(1) 0.4 V -> 1.4 V	1.66 ± 0.0169[c]	2.04 ± 0.0204[c]	1.48 ± 0.0156[c]	2.47 ± 0.0277[c]	2.91 ± 0.0424[c]	3.36 ± 0.0323[c]
	13.5 ± 0.0825[c]	17.7 ± 0.146[c]	16.6 ± 0.136[c]	19.9 ± 0.145[c]	31.0 ± 0.267[c]	26.8 ± 0.167[c]
(2) 1.4 V -> 0.4 V	3.06 ± 0.0169[c]	1.22 ± 0.00449[c]	2.48 ± 0.0105[c]	1.81 ± 0.0136[c]	0.511 ± 0.083[c]	3.03 ± 0.0104[c]
	48.2 ± 3.88[c]	37.6 ± 0.692[c]	59.0 ± 3.65[c]	26.4 ± 0.452[c]	5.0 ± 0.027[c]	(85.2)[c,d]

XAFS acquisition: (a) every 100 ms and (b) every 300 ms; Current acquisition: (c) every 20 ms; (d) tentative with large error bar.

wave cycling from 0.87 to 1.2 V_{RHE} in PEFC has also been estimated by a mathematical model.[60] The bond distances R(Pt-Pt) and R(Pt-O) did not change during the transient response processes. Consequently, in both potential operations the faster electrochemical process took place first, followed by the relatively slower electrochemical process, and in the similar time-scale to the slower electrochemical process the electronic and structural changes in the Pt catalysts (Pt charging/discharging, Pt-O bond formation/dissociation, and Pt-Pt bond dissociation/reformation) proceeded.

It is to be noted that there existed an isosbestic point around 11.570 keV in a series of XANES spectra for Pt/KB, Pt/AB and Pt/MWCNT similar to the previous Pt/C and PtM/C samples.[35] The presence of the isosbestic point indicates the direct transformation between an initial electronic state of Pt atoms at 0.4 V_{RHE} and a final electronic state at 1.4 V_{RHE} without any stable intermediate states in the transient response process. The isosbestic point in the XANES spectra was observed in both

increasing and the decreasing voltage operations, which suggests direct and reversible transformation between the two electronic states of Pt (metallic and PtO states) at 0.4 V_{RHE} and 1.4 V_{RHE}, respectively. It is also notable that the XANES spectra in the transient response processes were well fitted by a linear combination of the XANES spectra of Pt^0 foil and $Pt^{2+}O$, which also confirm the transformations of Pt nanoparticles between the two states as shown in Figure 8.

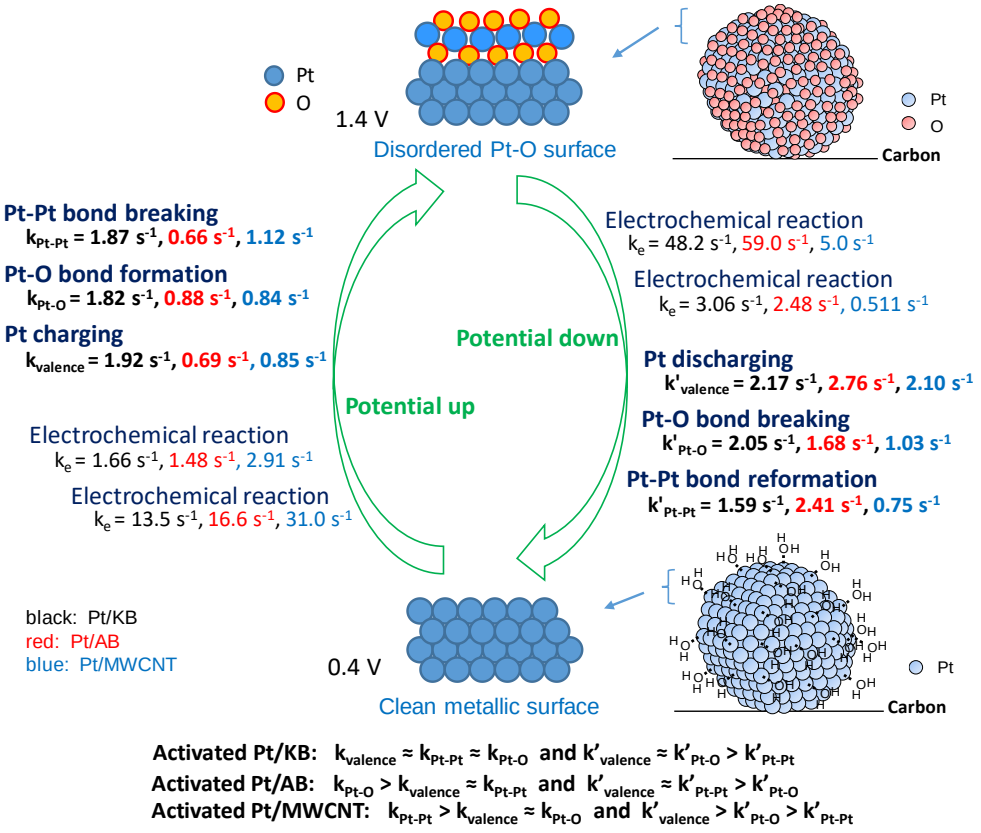

Figure 8. Reaction processes and their rate constants on Pt/KB (black), Pt/AB (red) and Pt/MWCNT (blue) cathode catalysts in activated MEAs in the voltage up (0.4 V_{RHE} -→ 1.4 V_{RHE}) and down (1.4 V_{RHE} -→ 0.4 V_{RHE}) cycle under H_2(anode)-N_2(cathode). The data after ADT cycles are not shown to avoid crowdedness.

The structural kinetics (the rate constants of the electronic and structural transformations: $k_{valence}$, k_{Pt-Pt} and k_{Pt-O}, and $k'_{valence}$, k'_{Pt-Pt} and k'_{Pt-O}) for the transient responses of the Pt valence, CN(Pt-Pt) and CN(Pt-O) on the potential operations for the Pt/KB, Pt/AB and Pt/MWCNT cathodes in MEAs is shown in Table 3 and Figure 8. As for the activated Pt/KB the rate constants (k) in the potential up operation (0.4 V_{RHE} → 1.4 V_{RHE}) were similar to each other, $k_{valence} \approx k_{Pt-Pt} \approx k_{Pt-O}$ and the rate constants (k') in the potential down operation (1.4 V_{RHE} → 0.4 V_{RHE}) changed in the order, $k'_{valence} \approx k'_{Pt-O} >$

$k'_{Pt\text{-}Pt}$. For the activated Pt/AB the order of the rate constants (k and k') were as follows, $k_{Pt\text{-}O} > k_{valence} \approx k_{Pt\text{-}Pt}$ and $k'_{valence} \approx k'_{Pt\text{-}Pt} > k'_{Pt\text{-}O}$. The rate constants for the activated Pt/MWCNT changed in the order, $k_{Pt\text{-}Pt} > k_{valence} \approx k_{Pt\text{-}O}$ and $k'_{valence} > k'_{Pt\text{-}O} > k'_{Pt\text{-}Pt}$. In general, the rate constants in the potential down operation were larger than those in the potential up operation though the rate constants $k'_{Pt\text{-}Pt}$ for Pt/KB and Pt/MWCNT were similar to or a little smaller than the corresponding rate constants $k_{Pt\text{-}Pt}$.

We also examined the structural kinetics of the Pt cathode catalysts for the transient voltage cycling processes between 0.4 V_{RHE} and 1.4 V_{RHE} under H_2 (anode)-Air (cathode), whose Pt L_{III}-edge time-resolved QXAFS spectra and transient response profiles are shown in ESI Figures S9-S11 and ESI Figures S16-S18, respectively. The rate constants are listed in ESI Table S2. Their time scales were approximately similar to those under H_2 (anode)-N_2 (cathode). The surface events and structural kinetics at the Pt cathodes under H_2 (anode)-Air (cathode) with a cell RH ~ 93% are essentially similar to those under H_2 (anode)-N_2 (cathode) with a cell RH ~ 93%. However, the difference in the structural parameters between 0.4 V_{RHE} and 1.4 V_{RHE} in air was smaller than that in N_2 particularly for the samples after the ADT cycles (ESI Table S1 and Table S2). Hence the structural kinetics under H_2 (anode)-Air (cathode) are not discussed in detail in this paper.

3.3. Relationships of the kinetic factors with the PEFC activity and durability. To find the structural kinetics of Pt/KB, Pt/AB and Pt/MWCNT in MEAs most relevant to the ORR activity (mass activity (MA) and surface specific activity (SA)), the rate constants $k_{valence}$, $k'_{valence}$, $k_{Pt\text{-}Pt}$, $k'_{Pt\text{-}Pt}$, $k_{Pt\text{-}O}$, and $k'_{Pt\text{-}O}$, respectively for Pt charging and discharging, Pt-Pt bond dissociation and reformation, and Pt-O bond formation and dissociation, which were determined by *in situ* time-resolved QXAFS analysis under H_2 (anode)-N_2 (cathode), were plotted against the MA and SA in Figure 9 (A) and (B), respectively. The rate constants and the activities were referred to those for the Pt/MWCNT, respectively. The rate enhancements of the structural kinetics ($k_{valence}$, $k_{Pt\text{-}Pt}$ and $k_{Pt\text{-}O}$) brought by the different carbon supports in the transient voltage increase (0.4 V_{RHE} → 1.4 V_{RHE}) were not proportional to the ORR activity as shown in Figure 9. The rate enhancement ($k'_{Pt\text{-}Pt}$) in the Pt-Pt bond reformation step in the transient voltage decrease (1.4 V_{RHE} → 0.4 V_{RHE}) was not proportional to the ORR activity, either. However, it was found that the rate enhancement ($k'_{Pt\text{-}O}$) in the Pt-O bond dissociation step in the transient voltage decrease (1.4 V_{RHE} → 0.4 V_{RHE}) showed the linear relationship with the MA and SA (Figure 9). The linear relationship between the $k'_{Pt\text{-}O}$ and the MA

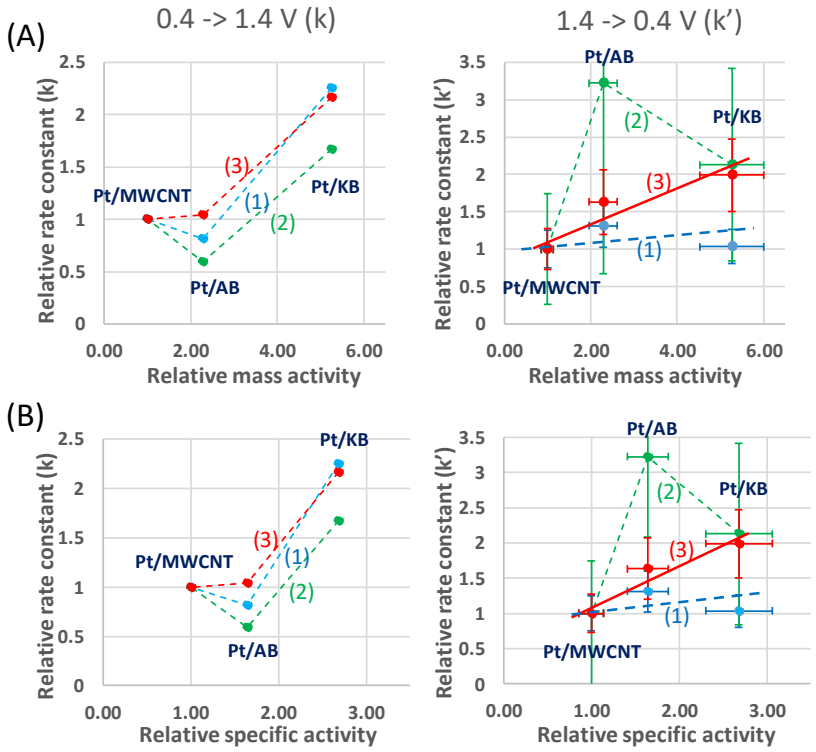

Figure 9. Relationship between the rate constants and the relative mass activities (A) or surface specific activities (B) for the Pt/KB, Pt/AB and Pt/MWCNT cathodes in activated MEAs. The rate constants for the Pt/KB and Pt/AB are the relative values to those for Pt/MWCNT. The relative mass activities and surface specific activities for the Pt/KB and Pt/AB are the relative values to those for Pt/MWCNT. (1) $k_{valence}$ or $k'_{valence}$; (2) $k_{Pt\text{-}Pt}$ or $k'_{Pt\text{-}Pt}$; (3) $k_{Pt\text{-}O}$ or $k'_{Pt\text{-}O}$.

and SA was also observed under H_2 (anode)-Air (cathode), and the linearity was also observed with the $k'_{valence}$ (not shown here). Thus, the blue dashed straight lines were tentatively drawn in Figure 9 under H_2 (anode)-N_2 (cathode). These aspects are similar to the alloy effect on the rate enhancement in the preceding work on Pt/KB, Pt_3Co/KB and Pt_3Ni/KB.[47,48] The reduction of oxygen species from the Pt surface is known to be key steps in the ORR sequence.[12,21,61-63] The present results indicated that the ORR rate enhancement is brought from the increase in the rate constants $k'_{Pt\text{-}O}$ (main) and $k'_{valence}$, resulting in easy reduction of Pt nanoparticles, which depended on the kind of carbon support. The *in situ* time-resolved QXAFS analysis provided direct information on the key structural kinetics of the Pt/C catalysts themselves for thorough understanding of the cathode catalysis toward PEFC improvement.

In addition to improving PEFC activity, long-term durability of the MEA cathode catalysts may be a more serious issue for widely spread commercialization of PEFC vehicles. It has been suggested that oxidative dissolution of Pt cathode catalysts is caused by a delay in Pt reduction in the practical potential changing processes.[64,65] We made plots of all rate constants obtained in this study against the MAs and SAs for the degraded Pt/KB, Pt/AB and Pt/MWCNT after the ADT cycles, but there was no relation among them (e.g. ESI Figure S19). Only the ratio of two rate constants $k'_{Pt\text{-}Pt}/k_{Pt\text{-}Pt}$ showed a linear relation with the durability of each cathode catalyst as shown in Figure 10, where the rate constants $k_{Pt\text{-}Pt}$ and $k'_{Pt\text{-}Pt}$ for each degraded sample are the relative values to those for each corresponding activated sample, respectively. The relative MA and SA of each degraded sample are also the relative values to those of each corresponding activated sample. The error range for the ratio k'/k was estimated by the equation ESI SI-2 and SI-3, where the error ranges are somewhat large due to a fraction (ratio). However, many XAFS measurements were conducted at SPring-8 as seen by a number of the beamtime proposal number in ACKNOWLEDGEMENT, and the linear relationship in Figure 10 was reproduced. The Pt/KB (ADT 1000), Pt/AB (ADT 5000) and Pt/MWCNT (ADT 5000), whose maximum power densities decreased similarly to about 55-60% of the initial values as described above, were used as the degraded samples to explore the key factors for the durability of Pt nanoparticles on KB, AB and MWCNT. The ratio $k'_{Pt\text{-}Pt}/k_{Pt\text{-}Pt}$ is a dimensionless quantity in contrast to the unit of s^{-1} in the $k'_{Pt\text{-}O}$ and $k'_{valence}$. The frequency (s^{-1}) as an indicator of the ORR activity may be convincing, while the measure of durability involves both $k_{Pt\text{-}Pt}$ and $k'_{Pt\text{-}Pt}$. Thus, the relative easiness of the recovery of a smooth metallic Pt surface at 0.4 V_{RHE} from the PtO layer at 1.4 V_{RHE} via the rough

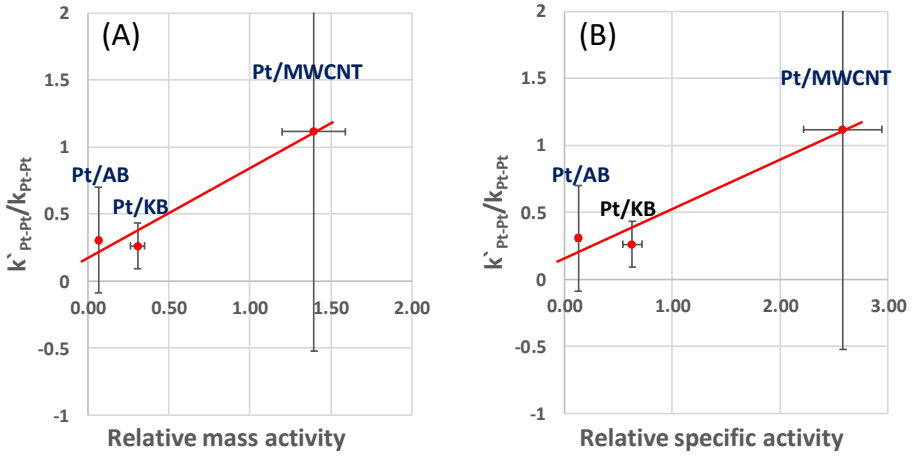

Figure 10. Relationship between the relative mass activities (A) or surface specific activities (B) and $k`_{Pt\text{-}Pt}/k_{Pt\text{-}Pt}$ for the Pt/KB, Pt/AB and Pt/MWCNT cathodes in MEAs after the ADT cycles. The rate constants $k_{Pt\text{-}Pt}$ and $k'_{Pt\text{-}Pt}$ for each sample after the ADT cycles are the relative values to those for each corresponding activated sample, respectively. The relative mass activities and surface specific activities for each sample after the ADT cycles are the relative values to those for each corresponding activated sample.

Pt surface, which is brought from the Pt-O bond dissociation,[7] is regarded to correlate with the durability of the MEA cathodes. The degradation reflects the balance of the rates of the dissociation and reformation of Pt-Pt bonds at the Pt surface layer. It should be noted that the present estimation for the MEA durability is not the estimation of the speeds of the decreases in the rate constants, MAs, and SAs as a function of the number of ADT cycles. In this study we have discussed on the structural kinetics under the transient potential operations for the degraded Pt/KB, Pt/AB, and Pt/MWCNT cathodes at about 55-60% levels of the initial power densities, which were compared to the structural kinetics for the activated Pt/KB, Pt/AB, and Pt/MWCNT.

Finally, we examined if there is the key factor in the structural kinetics for the activated cathode catalysts, by which we can predict the durability of the cathode catalysts in MEAs without durability tests for many hours. We found a good relationship between $1/k'_{Pt\text{-}Pt}$ for the activated MEAs and the relative MA and SA as shown in Figure 11 (blue line (1)). The linear relationship was confirmed by separate XAFS measurements as mentioned above. The $k'_{Pt\text{-}Pt}$ is the rate constants for the Pt-Pt bond reformation in the activated Pt/KB, Pt/AB, and Pt/MWCNT under the transient potential operation (1.4 $V_{RHE} \rightarrow$ 0.4 V_{RHE}), while the relative MA and SA of each sample are the relative values for the degraded samples to the ones for the activated samples. The inverse of $k'_{Pt\text{-}Pt}$ means a relaxation time (in second) of the Pt-Pt bond reformation process under the transient potential operation (1.4 $V_{RHE} \rightarrow$

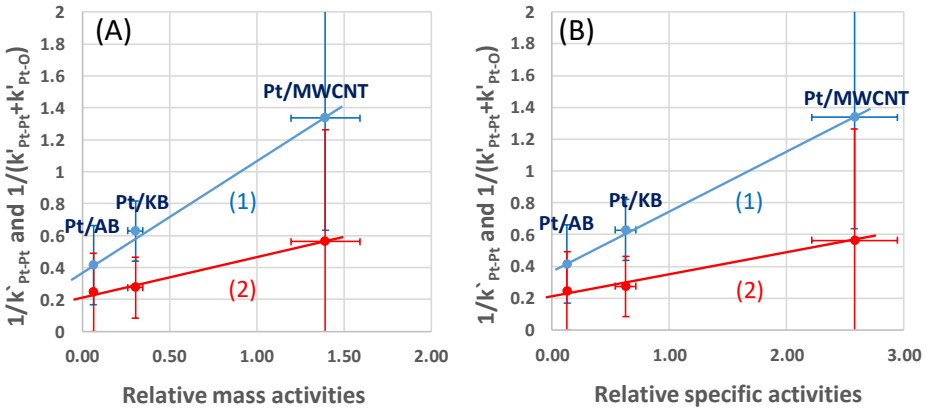

Figure 11. Relationship between the relative mass activities (A) or surface specific activities (B) after the ADT cycles (Figure 9) and $1/k'_{Pt\text{-}Pt}$ (1) or $1/(k'_{Pt\text{-}Pt}+k'_{Pt\text{-}O})$ (2) for the Pt/KB, Pt/AB and Pt/MWCNT cathodes in activated MEAs. The rate constants $k'_{Pt\text{-}Pt}$ and $k'_{Pt\text{-}O}$ are the values for each activated sample, respectively. The relative mass activities and surface specific activities of each sample after the ADT cycles are the relative values to those of each corresponding activated sample.

0.4 V_{RHE}). The larger the relaxation time for the Pt-Pt bond reformation, the longer the durability becomes. We also found a good relationship between $1/(k'_{Pt\text{-}Pt}+k'_{Pt\text{-}O})$ and the relative MA and SA as shown in Figure 11 (red line (2)). A good linearity was not observed with the $1/k'_{Pt\text{-}O}$ alone, and hence the Pt-Pt bond reformation rather than the Pt-O bond dissociation is more relevant to the durability. These results demonstrate that the Pt/MWCNT with the largest relaxation time for the Pt-Pt bond reformation shows the highest durability. However, the Pt/MWCNT shows the lowest ORR activity due to the smallest $k'_{Pt\text{-}O}$ among Pt/KB, Pt/AB and Pt/MWCNT as shown in Figure 9. Materialization of decreasing the $k'_{Pt\text{-}Pt}$ and increasing the $k'_{Pt\text{-}O}$ simultaneously is demanded for improvements of both activity and durability, but this may be a dilemma because the Pt-Pt bond reformation and Pt-O bond dissociation may not proceed independently. The whole behavior of PEFC performances during the triangular ADT cycles should be more complex involving heterogeneous carbon corrosion in addition to the structural kinetics of Pt nanoparticles in MEAs. Both time-resolved and spatially-resolved XAFS techniques may be powerful for understanding of the more detailed PEFC degradation. Further investigation on other different types of cathode catalysts in MEAs is needed to confirm if the present approach and conclusion can be universally utilized in the development of PEFC cathode catalysts with high durability.

4. CONCLUSIONS

We have investigated a series of *in situ* time-resolved QXAFS spectra (100 ms/spectrum) of Pt/KB, Pt/AB, and Pt/MWCNT in PEFC MEAs under transient potential operations (0.4 V_{RHE} → 1.4 V_{RHE} → 0.4 V_{RHE}), while measuring the electrochemical current/charge at the cathode. The ORR rate enhancement depended on the kind of carbon supports. Detailed QEXAFS analysis revealed the potential-dependent surface structures at 0.4 V_{RHE} and 1.4 V_{RHE}. The structural kinetics of elementary reaction steps at the cathode Pt surface in the transient potential operations under H_2 (anode)-N_2 (cathode) and H_2 (anode)-air (cathode) was explored to determine the rate constants for charging ($k_{valence}$)/discharging ($k'_{valence}$) of cathode Pt nanoparticles, Pt-O bond formation ($k_{Pt\text{-}O}$)/dissociation ($k'_{Pt\text{-}O}$) and Pt-Pt bond dissociation ($k_{Pt\text{-}Pt}$)/reformation ($k'_{Pt\text{-}Pt}$). The rate enhancements ($k'_{Pt\text{-}O}$ and $k'_{valence}$) in the Pt-O bond dissociation and Pt valence change processes under the transient potential operation (1.4 V_{RHE} → 0.4 V_{RHE}) showed the linear relationship with the mass activity (MA) and surface specific activity (SA). It was found that the ratio $k'_{Pt\text{-}Pt}/k_{Pt\text{-}Pt}$ for the degraded MEAs after ADT cycles, relative to that for the activated MEAs, showed a linear relationship with the durability of Pt/KB, Pt/AB, and Pt/MWCNT. We also found a good relationship between $1/k'_{Pt\text{-}Pt}$ and $1/(k'_{Pt\text{-}Pt}+k'_{Pt\text{-}O})$ for the activated MEAs and the relative MAs and SAs for the degraded MEAs. The relaxation time of the Pt-Pt bond reformation and Pt-O bond dissociation processes in the activated MEAs may predict the relative durability of the similar kinds of cathode catalysts without durability tests. *In situ* time-resolved QXAFS is a promising technique which can aid the further improvement of PEFC performance and durability for development of the next-generation PEFCs.

Running title:

Key Structural Kinetics for the Pt/C Catalysts in MEA by *In Situ* Time-Resolved XAFS

ASSOCIATED CONTENT

Electronic Supplementary Information (ESI) available via the Internet at http://pubs.acs.org.

Experimental procedures, electrochemical data, structural models by estimated coordination numbers, series of time-resolved QXANES spectra and QEXAFS Fourier transforms in H_2(anode)-N_2(cathode) and H_2(anode)- air(cathode), curve fitting results.

AUTHOR INFORMATION

Corresponding Author

* Yasuhiro Iwasawa

Tel: +81-42-443-5921; E-mail: iwasawa@pc.uec.ac.jp

Author Contributions

The manuscript was written through contributions of all authors. All authors have given approval to the final version of the manuscript.

Conflict of Interest

The authors declare no competing financial interest.

ACKNOWLEDGMENT

This work was supported by the New Energy and Industrial Technology Development Organization (NEDO) of the Ministry of Economy, Trade, and Industry (METI), Japan. XAFS measurements were conducted at SPring-8 for several years (No. 2011B1015 (BL01B1), 2011B1017 (BL40XU), 2011B1038 (BL40XU), 2012A1004 (BL40XU), 2012A1013 (BL40XU), 2012A1014 (BL01B1), 2012B1022 (BL01B1), 2013A7801 (BL36XU), 2013A7802 (BL36XU), 2013B7806 (BL36XU), 2014A7801 (BL36XU), 2014B7803 (BL36XU), 2015A7803 (BL36XU), 2015A7804 (BL36XU), 2015B7805 (BL36XU), 2015B7801 (BL36XU), 2015B7803 (BL36XU), 2016A7802 (BL36XU).

REFERENCES

(1) Debe, K. Electrocatalyst Approaches and Challenges for Automotive Fuel Cells. *Nature* **2012**, *486*, 43−51.

(2) Zhang, L.; Roling, L. T.; Wang, X.; Vara, M. V.; Chi, M.; Liu, J.; Choi, S.; Park, J.; Herron, J. A.; Xie, Z.; et al. Platinum-Based Nanocages with Subnanometer-Thick Walls and Well-Defined, Controllable Facets. *Science* **2015**, *349*, 412-416.

(3) Escudero-Escribano, M.; Malacrida, P.; Hansen, M. H.; Vej-Hansen, U. G.; Velázquez-Palenzuela, A.; Tripkovic, V.; Schiøtz, J.; Rossmeisl, J.; Stephens, I. E. L.; Chorkendorff, I. Tuning the Activity of Pt Alloy Electrocatalysts by Means of the Lanthanide Contraction. *Science* **2016**, *352*, 73-76.

(4) Oezaslan, M.; Hasché, F.; Strasser, P. Pt-Based Core–Shell Catalyst Architectures for Oxygen Fuel Cell Electrodes. *J. Phys. Chem. Lett.* **2013**, *4*, 3273−3291.

(5) Mistry, H.; Varela A. S.; Kühl, S.; Strasser, P.; Cuenya, B. R. Nanostructured Electrocatalysts with Tunable Activity and Selectivity. *Nature Rev. Materials*, **2016**, DOI: 10.1038/natrevmats.2016.9.

(6) Nagasawa, K.; Takao, S.; Nagamatsu, S.; Samjeské, G.; Sekizawa, O.; Kaneko, T.; Higashi, K.; Yamamoto, T.; Uruga, T.; Iwasawa, Y. Surface-Regulated Nano-SnO_2/Pt_3Co/C Cathode Catalysts for Polymer Electrolyte Fuel Cells Fabricated by a Selective Electrochemical Sn Deposition Method. *J. Am. Chem. Soc.* **2015**, *137*, 12856−12864.

(7) Tada, M.; Uruga, T.; Iwasawa, Y. Key Factors Affecting the Performance and Durability of Cathode Electrocatalysts in Polymer Electrolyte Fuel Cells Characterized by In Situ Real Time and Spatially Resolved XAFS Techniques. *Catal. Lett. (Silver Anniversary Special Issue)* **2015**, *145*, 58-70.

(8) Chen, C.; Kang, Y.; Huo, Z.; Zhu, Z.; Huang,W.; Huolin, W.; Xin, L.; Snyder, J. D.; Li, D.; Herron, J. A.; et al. Highly Crystalline Multimetallic Nanoframes with Three-Dimensional Electrocatalytic Surfaces. *Science* **2014**, *343*, 1339-1343.

(9) Rabis, A; Rodriguez, P; Schmidt, T. J. Electrocatalysis for Polymer Electrolyte Fuel Cells: Recent Achievements and Future Challenges. *ACS Catal.* **2012**, *2*, 864−890.

(10) Wu, G.; More, K. L.; Johnston, C. M.; Zelenay, P. High-Performance Electrocatalysts for Oxygen Reduction Derived from Polyaniline, Iron, and Cobalt. *Science* **2011,** *332*, 443−447.

(11) Borup, R.; Meyers, J.; Pivovar, B.; Kim, Y. S.; Mukundan, R.; Garland, N.; Myers, D.; Wilson, M.; Garzon, F.; Wood, D.; et al. Scientific Aspects of Polymer Electrolyte Fuel Cell Durability and Degradation. *Chem. Rev.* **2007**, *107*. 3904−3951.

(12) Stamenkovic, V. R.; Fowler, B.; Mun, B. S.; Wang, G.; Ross, P. N.; Lucas, C. A.; Marcovic, N. M. Improved Oxygen Reduction Activity on Pt_3Ni(111) via Increased Surface Site Availability. *Science* **2007**, *315*, 493−497.

(13) Strasser, P.; Koh, S.; Anniyev, T.; Greeley, J.; More, K.; Yu, C.; Liu, Z.; Kaya, S.; Nordlund, D.; Ogasawara, H.; et al. Lattice-Strain Control of the Activity in Dealloyed Core–Shell Fuel Cell Catalysts. *Nature Chem.* **2010**, *2*, 454-460.

(14) Wu, J.; Yang, H. Platinum-Based Oxygen Reduction Electrocatalysts. *Acc. Chem. Res*. **2013**, *46*, 1848-1857.

(15) Dresselhaus, M. S.; Thomas, I. L. Alternative Energy Technologies. *Nature* **2001**, *414*, 332-337.

(16) Weber, A. Z.; Newman, J. Modeling Transport in Polymer-Electrolyte Fuel Cells. *Chem. Rev.* **2004**, *104*, 4679-4726.

(17) Wang, C. Y. Fundamental Models for Fuel Cell Engineering. *Chem. Rev.* **2004**, *104*, 4727–4766.

(18) Jacobson, M. Z.; Colella W. G.; Golden, D. M. Cleaning the Air and Improving Health with Hydrogen Fuel-Cell Vehicles. *Science* **2005**, *308*, 1901-1905.

(19) Steele, B. C. H; Heinzel, A. Materials for Fuel-Cell Technologies. *Nature* **2001**, *414*, 345-352.

(20) Huang, Y. H.; Dass, R. I.; Xing, Z. L.; Goodenough, J. B. Double Perovskites as Anode Materials for Solid-Oxide Fuel Cells. *Science* **2006**, *312*, 254-257.

(21) Stamenkovic, V.; Mun, B. S.; Mayrhofer, K. J. J.; Ross, P. N.; Markovic, N. M.; Rossmeisl, J.; Greeley, J.; Norskov, J, K. Changing the Activity of Electrocatalysts for Oxygen Reduction by Tuning the Surface Electronic Structure. *Angew. Chem. Int. Ed.* **2006**, *45*, 2897–2901.

(22) Shao, Z. P.; Haile, S. M.; Ahn, J.; Ronney, P. D.; Zhan, Z. L.; Barnett, S. A. A Thermally Self-Sustained Micro Solid-Oxide Fuel-Cell Stack with High Power Density. *Nature* **2005**, *435*, 795-798.

(23) DOE, Fuel Cell Technical Team Roadmap, June 2013; www.vehicles.energy.gov/about/partnerships/usdrive.html or www.uscar.org.

(24) Iwasawa, Y.; Asakura, K.; Ishii, H.: Kuroda, H. Dynamic Behaviour of Active Sites of a SiO_2-Attached Mo(VI)-Dimer Catalyst during Ethanol Oxidation Observed by Means of EXAFS. *Z. Phys. Chem. N. F.* **1985**, *144*, 105-115.

(25) Iwasawa, Y. Chemical Design Surfaces for Active Solid Catalysts. *Adv. Catal.* **1987**, *35*, 187-264.

(26) Iwasawa, Y. *X-ray Absorption Fine Structure for Catalysts and Surfaces*; World Scientific Publishing: Singapore, 1996.

(27) Iwasawa, Y.; Asakura, K.; Tada, M. *XAFS Techniques for Catalysts, Nanomaterials and Surfaces*; Springer: New York, 2016.

(28) Asakura, K.; Bando, K. K.; Iwasawa, Y.; Arakawa, H.; Isobe, K. Metal-Assisted Hydroformylation on a SiO_2-Attached Rhodium Dimer. In Situ EXAFS and FT-IR Observations of the Dynamic Behaviors of the Dimer Site. *J. Am. Chem. Soc.* **1990**, *112*, 9096-9104.

(29) Izumi, Y.; Chihara, T.; Yamazaki, H.; Iwasawa, Y. Carbon Monoxide-Breathing Ruthenium Carbido Clusters on Magnesium Oxide (MgO) in CO/H_2 Reaction Conditions. *J. Am. Chem. Soc.* **1993**, *115*, 6462-6463.

(30) Mukerjee, S.; Srinivasan, S.; Soriaga, M. P.; McBreen, J. Role of Structural and Electronic Properties of Pt and Pt Alloys on Electrocatalysis of Oxygen Reduction: An in Situ XANES and EXAFS Investigation. *J. Electrochem. Soc.* **1995**, *142*, 1409-1422.

(31) Weckhuysen, B. M. Determining the Active Site in a Catalytic Process: Operando Spectroscopy is More than a Buzzword. *Phys. Chem. Chem. Phys*. **2003**, *5*, 4351–4360.

(32) Singh, J.; Lamberti, C.; van Bokhoven, J. A. Advanced X-ray Absorption and Emission Spectroscopy: In Situ Catalytic Studies. *Chem. Soc. Rev.* **2010**, *39*, 4754–4766.

(33) Friebel, D.; Viswanathan, V.; Miller, D. J.; Anniyev, T.; Ogasawara, H.; Larsen, A. H.; O'Grady, C. P.; Nørskov, J. K.; Nilsson, A. Balance of Nanostructure and Bimetallic Interactions in Pt Model Fuel Cell Catalysts: In Situ XAS and DFT Study. *J. Am. Chem. Soc*. **2012**, *134*, 9664-9671.

(34) Adzic, R. R.; Wang, J. X.; Ocko, B. M.; McBreen, J. *EXAFS, XANES, SXS. Handbook of Fuel Cells*; Wiley: Online, 2010.

(35) Nagamatsu, S.; Arai, T.; Yamamoto, M.; Ohkura, T.; Oyanagi, H.; Ishizaka, T.; Kawanami, H.; Uruga, T.; Tada, M.; Iwasawa, Y. Potential-Dependent Restructuring and Hysteresis in the Structural and Electronic Transformations of Pt/C, Au(Core)-Pt(Shell)/C, and Pd(Core)-Pt(Shell)/C Cathode Catalysts in Polymer Electrolyte Fuel Cells Characterized by in Situ X-ray Absorption Fine Structure. *J. Phys. Chem. C* **2013**, *117*, 13094-13107.

(36) Samjeské, G.; Higashi, K.; Takao, S.; Nagamatsu, S.; Nagasawa, K.; Sekizawa, O.; Kaneko, T.; Uruga, T.; Iwasawa,Y. In Situ Techniques to Study the Effects of Anode or Cathode Gas-Exchange Cycles on the Deterioration of Pt/C Cathode Catalysts in PEFCs. *ChemElectroChem* **2015**, *2*, 1595-1606.

(37) Nagasawa, K.; Takao, S.; Higashi, K.; Nagamatsu, S.; Samjeské, G.; Imaizumi, Y.; Sekizawa, O.; Yamamoto, T.; Uruga, T.; Iwasawa,Y. Performance and Durability of Pt/C Cathode Catalysts with Different Kinds of Carbons for Polymer Electrolyte Fuel Cells Characterized by

Electrochemical and in Situ XAFS Techniques. *Phys. Chem. Chem. Phys*. **2014**, *16*, 10075-10087.

(38) Nagamatsu, S.; Takao, S.; Samjeské, G.; Nagasawa, K.; Sekizawa, O.: Kaneko, T.; Higashi, K.; Uruga, T.; Gayen, S.; Velaga, S.; et al. Structural and Electronic Transformations of Pt/C, Pd@Pt(1 ML)/C and Pd@Pt(2 ML)/C Cathode Catalysts in Polymer Electrolyte Fuel Cells during Potential-Step Operating Processes Characterized by in-Situ Time-resolved XAFS. *Surf. Sci.* **2016**, *648*, 100-113.

(39) Iwasawa, Y. In Situ Characterization of Supported Metal Catalysts and Model Surfaces by Time-Resolved and Three-Dimensional XAFS Techniques. *J .Catal*. **2003**, *216*, 165-177.

(40) Suzuki, A.; Inada, Y.; Yamaguchi, A.; Chihara, T.; Yuasa, M.; Nomura, M.; Iwasawa, Y. Time Scale and Elementary Steps of CO-Induced Disintegration of Surface Rhodium Clusters. *Angew. Chem. Int. Ed*. **2003**, *42*, 4795-4799.

(41) Yamamoto, T.; Suzuki, A.; Nagai, Y.; Tanabe, T.; Dong, F.; Inada, Y.; Nomura, M.; Tada, M.; Iwasawa, Y. Origin and Dynamics of Oxygen Storage/Release in a Pt/Ordered CeO_2–ZrO_2 Catalyst Studied by Time-Resolved XAFS Analysis. *Angew. Chem. Int. Ed.* **2007**, *46*, 9253-9256.

(42) Tada, M.; Uemura, Y.; Bal, R.; Inada, Y.; Nomura, M.; Iwasawa, Y. In Situ Time-Resolved DXAFS for the Determination of Kinetics of Structural Changes of H-ZSM-5-Supported Active Re-Cluster Catalyst in the Direct Phenol Synthesis from Benzene and O_2. *Phys. Chem. Chem. Phys.* **2010**, *12*, 5701–5706.

(43) Uemura, Y.; Inada, Y.; Bando, K. K.; Sasaki, T.; Kamiuchi, N.; Eguchi, K.; Yagishita, A.; Nomura, M.; Tada, M.; Iwasawa, Y. Core−Shell Phase Separation and Structural Transformation of Pt_3Sn Alloy Nanoparticles Supported on γ-Al_2O_3 in the Reduction and Oxidation Processes Characterized by In Situ Time-Resolved XAFS. *J. Phys. Chem. C* **2011**, *115*, 5823-5833.

(44) Uemura, Y.; Inada, Y.; Bando, K. K.; Sasaki, T.; Kamiuchi, N.; Eguchi, K.; Yagishita, A.; Nomura, M.; Tada, M.; Iwasawa, Y. In Situ Time-Resolved XAFS Study on the Structural Transformation and Phase Separation of Pt_3Sn and PtSn Alloy Nanoparticles on Carbon in the Oxidation Process. *Phys. Chem. Chem. Phys*. **2011**, *13*, 15833-15844.

(45) Tada, M.; Murata, S.; Asaoka, T.; Hiroshima, K.; Okumura, K.; Tanida, H.; Uruga, T.; Nakanishi, H.; Matsumoto, S.; Inada, Y.; et al. In Situ Time-Resolved Dynamic Surface Events on the Pt/C Cathode in a Fuel Cell under Operando Conditions. *Angew. Chem. Int. Ed.* **2007**, *46*, 4310-4315.

(46) Ishiguro, N.; Saida, T.; Uruga, T.; Nagamatsu, S.; Sekizawa, O.; Nitta, K.; Yamamoto, T.; Ohkoshi, S.; Yokoyama, T.; Tada, M; et al. Operando Time-Resolved X-ray Absorption Fine Structure Study for Surface Events on a Pt_3Co/C Cathode Catalyst in a Polymer Electrolyte Fuel Cell during Voltage-Operating Processes. *ACS Catal.* **2012**, *2*, 1319-1330.

(47) Ishiguro, N.; Kityakarn, S.; Sekizawa, O.; Uruga, T.; Sasabe, T.; Nagasawa, K.; Yokoyama, T.; Tada, M. Rate Enhancements in Structural Transformations of Pt–Co and Pt–Ni Bimetallic Cathode Catalysts in Polymer Electrolyte Fuel Cells Studied by in Situ Time-Resolved X-ray Absorption Fine Structure. *J. Phys. Chem. C* **2014**, *118*, 15874-15883.

(48) Ishiguro, N.; Saida, T.; Uruga, T.; Sekizawa, O.; Nagasawa, K.: Nitta, K.; Yamamoto, T.; Ohkoshi, S.; Yokoyama, T.; Tada, M. Structural Kinetics of a Pt/C Cathode Catalyst with Practical Catalyst Loading in an MEA for PEFC Operating Conditions Studied by in Situ Time-Resolved XAFS. *Phys. Chem. Chem. Phys.* **2013**, *15*, 18827-18834.

(49) Sekizawa, O.; Uruga, T.; Tada, M.; Nitta, K.; Kato, K.; Tanida, H.; Takeshita, K.; Takahashi, S.; Sano, M.; M.; Aoyagi, H.; et al. New XAFS Beamline for Structural and Electronic Dynamics of Nanoparticle Catalysts in Fuel Cells under Operating Conditions. *J. Phys., Conf. Ser.* **2013**, *430*, 012020-1-4.

(50) Newville, M.; Ravel, B.; Haskel, D.; Rehr, J. J.; Stern, E. A.; Yacoby, Y. Analysis of Multiple-Scattering XAFS Data Using Theoretical Standards. *Phys. B* **1995**, *208–209*, 154-156.

(51) Ravel, B.; Newville, M. ATHENA, ARTEMIS, HEPHAESTUS: Data Analysis for X-ray Absorption Spectroscopy Using IFEFFIT. *J. Synchrotron Rad.* **2005**, *12*, 537-541.

(52) Rehr J. J.; Albers, R. C. Theoretical Approaches to X-ray Absorption Fine Structure. *Rev. Mod. Phys.* **2000**, *72*, 621-654.

(53) Shao, M.; Peles A.; Shoemaker, K. Electrocatalysis on Platinum Nanoparticles: Particle Size Effect on Oxygen Reduction Reaction Activity. *Nano Lett.*, **2011**, *11*, 3714-3719.

(54) Gasteiger, H. A.; Kocha, S. S.; Sompalli, B.; Wagner, F. T. Activity Benchmarks and Requirements for Pt, Pt-alloy, and Non-Pt Oxygen Reduction Catalysts for PEMFCs. *Appl. Catal. B*, **2005**, *56*, 9-35.

(55) Li, Y.; Frenkel, A. I. Metal Nanocatalysts. In *XAFS Techniques for Catalysts, Nanomaterial, and Surfaces*; Iwasawa, Y.; Asakura, K.; Tada, M. Eds.; Springer: New York, 2016.

(56) Benfield, R. E. Mean Coordination Numbers and the Non-Metal–Metal Transition in Clusters. *J. Chem. Soc. Faraday Trans*. **1992**, *88*, 1107-1110.

(57) Jentys, A. Estimation of Mean Size and Shape of Small Metal Particles by EXAFS. *Phys. Chem. Chem. Phys.* **1999**, *1*, 4059-4063.

(58) Friebel, D.; Miller, D. J.; O'Grady, C. P.; Anniyev, T.; Bargar, J.; Bergmann, U.; Ogasawara, H.; Wikfeldt, K. T.; Pettersson, L. G. M.; Nilsson, A. In Situ X-ray Probing Reveals Fingerprints of Surface Platinum Oxide. *Phys. Chem. Chem. Phys.* **2011**, *13*, 262–266.

(59) Uribe, F. A.; Zawodzinski, T. A. A Study of Polymer Electrolyte Fuel Cell Performance at High Voltages. Dependence on Cathode Catalyst Layer Composition and on Voltage Conditioning. *Electrochim. Acta* **2002**, *47*, 3799-3806.

(60) Darling, R. M.; Meyers, J. P. Mathematical Model of Platinum Movement in PEM Fuel Cells. *J. Electrochem. Soc.* **2005**, *152*, A242-A247.

(61) Stamenkovic, V. R.; Mun, B. S.; Arenz, M.; Mayrhofer, K. J. J.; Lucas, C. A.; Wang, G.; Ross, P. N.; Marcovic, N. M. Trends in Electrocatalysis on Extended and Nanoscale Pt-Bimetallic Alloy Surfaces. *Nat. Mat.*, **2007**, *6*, 241-247.

(62) Hirunsit, P.; Balbuena, P. B. Effects of Water and Electric Field on Atomic Oxygen Adsorption on Pt–Co Alloys. *Surf. Sci.*, **2009**, *603*, 3239-3248.

(63) Matanovic, I.; Garzon, F. H.; Henson, N. J. Theoretical Study of Electrochemical Processes on Pt–Ni Alloys. *J. Phys. Chem. C* **2011**, *115*, 10640-10650.

(64) Yu, P.; Pemberton, M.; Plasse, P. PtCo/C Cathode Catalyst for Improved Durability in PEMFCs. *J. Power Sources*, **2005**, *144*, 11-20.

(65) Colon-Mercado, H. R.; Popov, B. N. Stability of Platinum Based Alloy Cathode Catalysts in PEM Fuel Cells. *J. Power Sources*, **2006**, *155*, 253-263.

Table of Contents Graphic

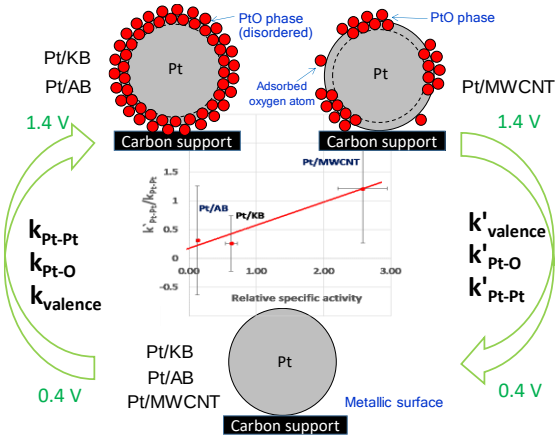

Supporting Information

Key Structural Kinetics for Carbon Effects on the Performance and Durability of Pt/Carbon Cathode Catalysts in Polymer Electrolyte Fuel Cells Characterized by *In Situ* Time-Resolved XAFS

Takuma Kaneko,[†] Gabor Samjeské,[†] Shin-ichi Nagamatsu,[†] Kotaro Higashi,[†] Oki Sekizawa,[†] Shinobu Takao,[†] Takashi Yamamoto,[‡] Xiao Zhao,[†] Tomohiro Sakata,[†] Tomoya Uruga,[†, §] and Yasuhiro Iwasawa[†, #]*

[†] Innovation Research Center for Fuel Cells, The University of Electro-Communications, Chofugaoka, Chofu, Tokyo 182-8585, Japan

[‡] Department of Mathematical and Material Sciences, The University of Tokushima, Minamijosanjima, Tokushima 770-8502, Japan

[§] Japan Synchrotron Radiation Research Institute, SPring-8, Sayo, Hyogo 679-5198, Japan

[#] Graduate School of Infotmatics and Engineering, The University of Electro-Communications, Chofugaoka, Chofu, Tokyo 182-8585, Japan

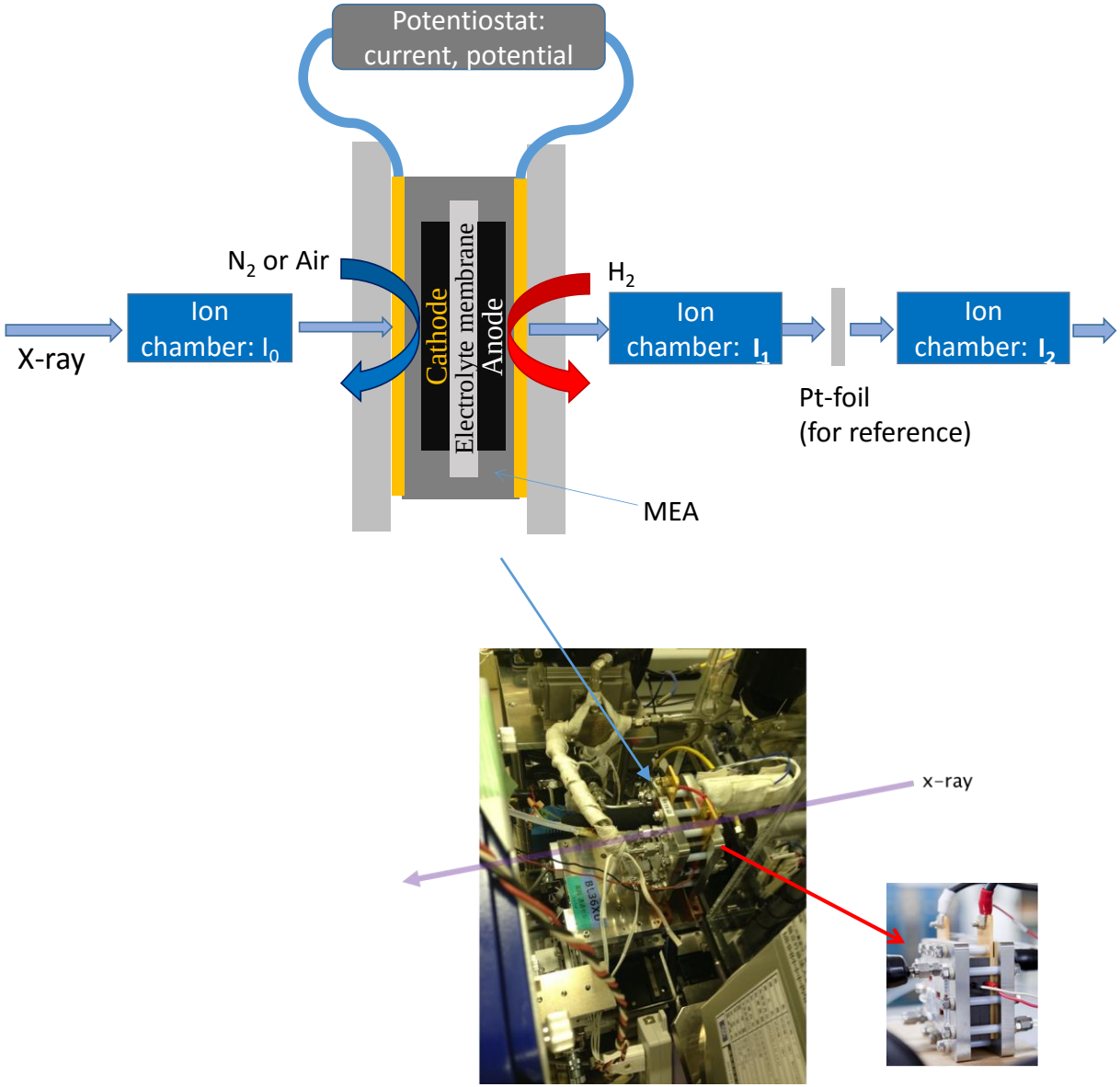

Figure S1. Experimental setup for *in situ* time-resolved XAFS measurements, while measuring the current/charge of PEFC during the operating processes. The similar setup and XAFS cell were used in refs. 34-38.

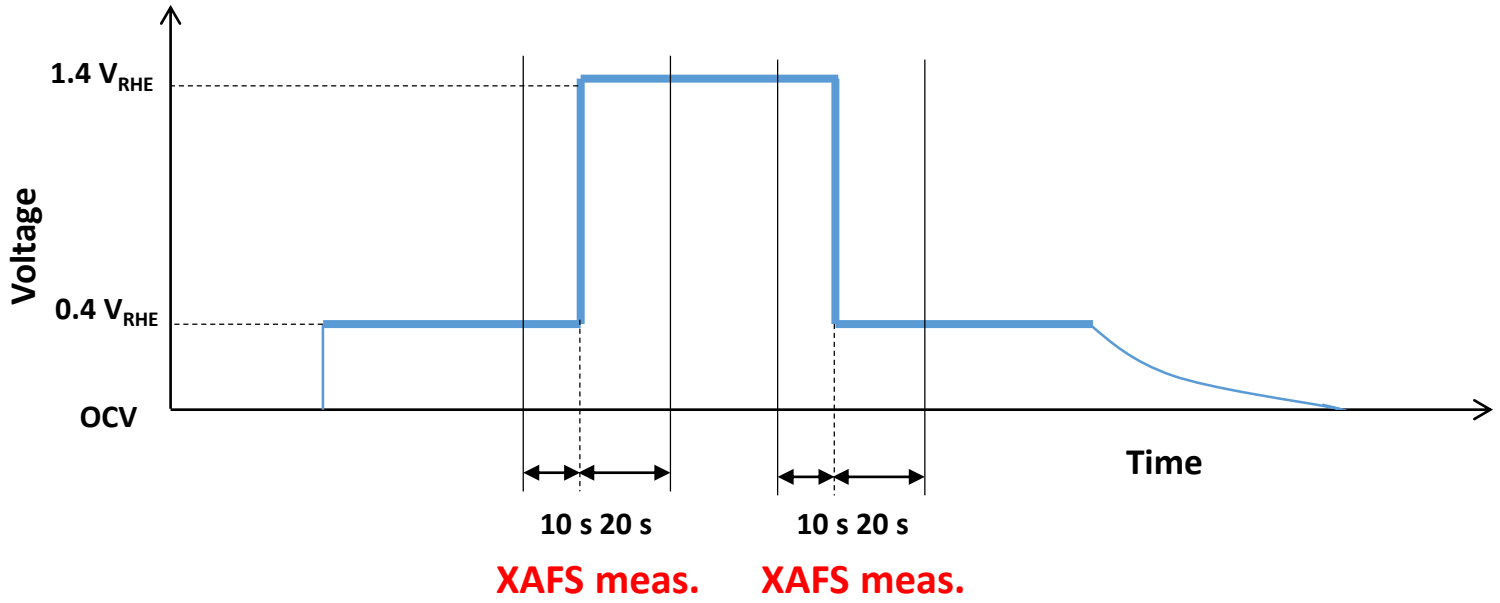

Figure S2. The transient potential-jump operation (0.4 V_{RHE} -> 1.4 V_{RHE}) and –down operation (1.4 V_{RHE}-> 0.4 V_{RHE}) operations at the cathode in PEFC and the period of the transient-response XAFS measurements at Pt L_{III}-edge (100 ms/spectrum).

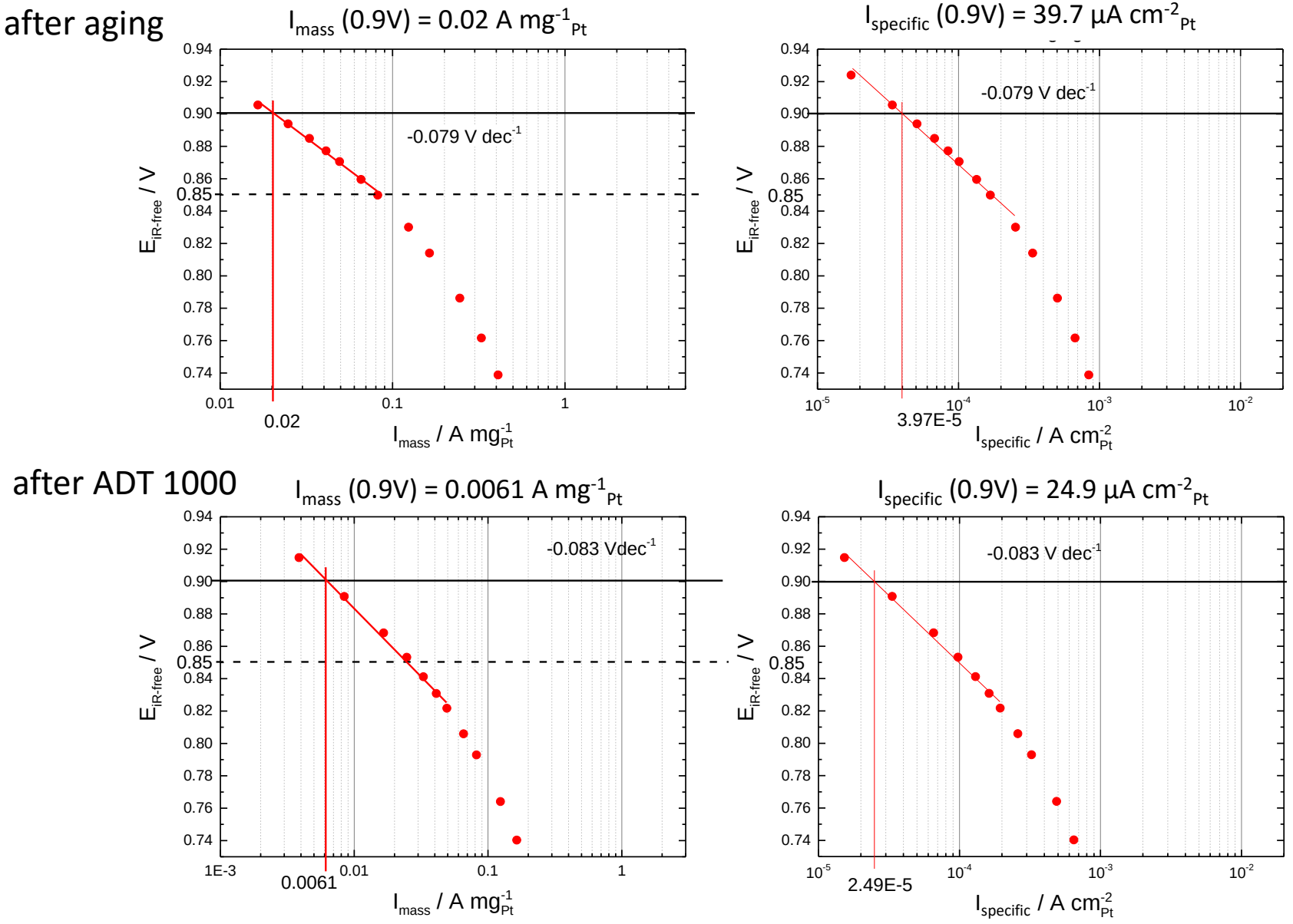

Figure S3. Mass activities and surface specific activities for MEA Pt/KB after the conditioning (activating) and ADT 1000 cycles by semi-logarithmic plots of I-V polarization curves.

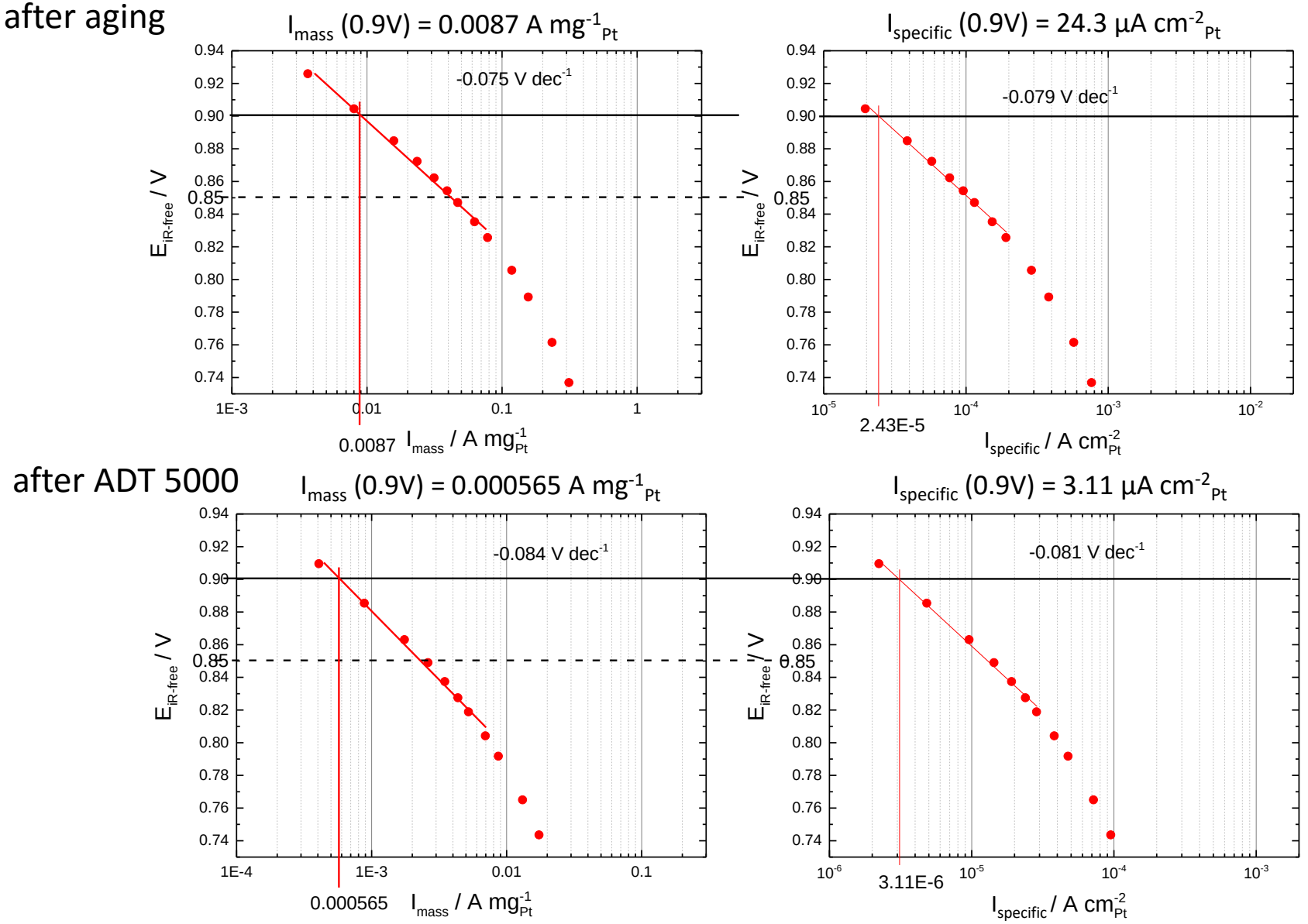

Figure S4. Mass activities and surface specific activities for MEA Pt/AB after the conditioning (activating) and ADT 5000 cycles by semi-logarithmic plots of I-V polarization curves.

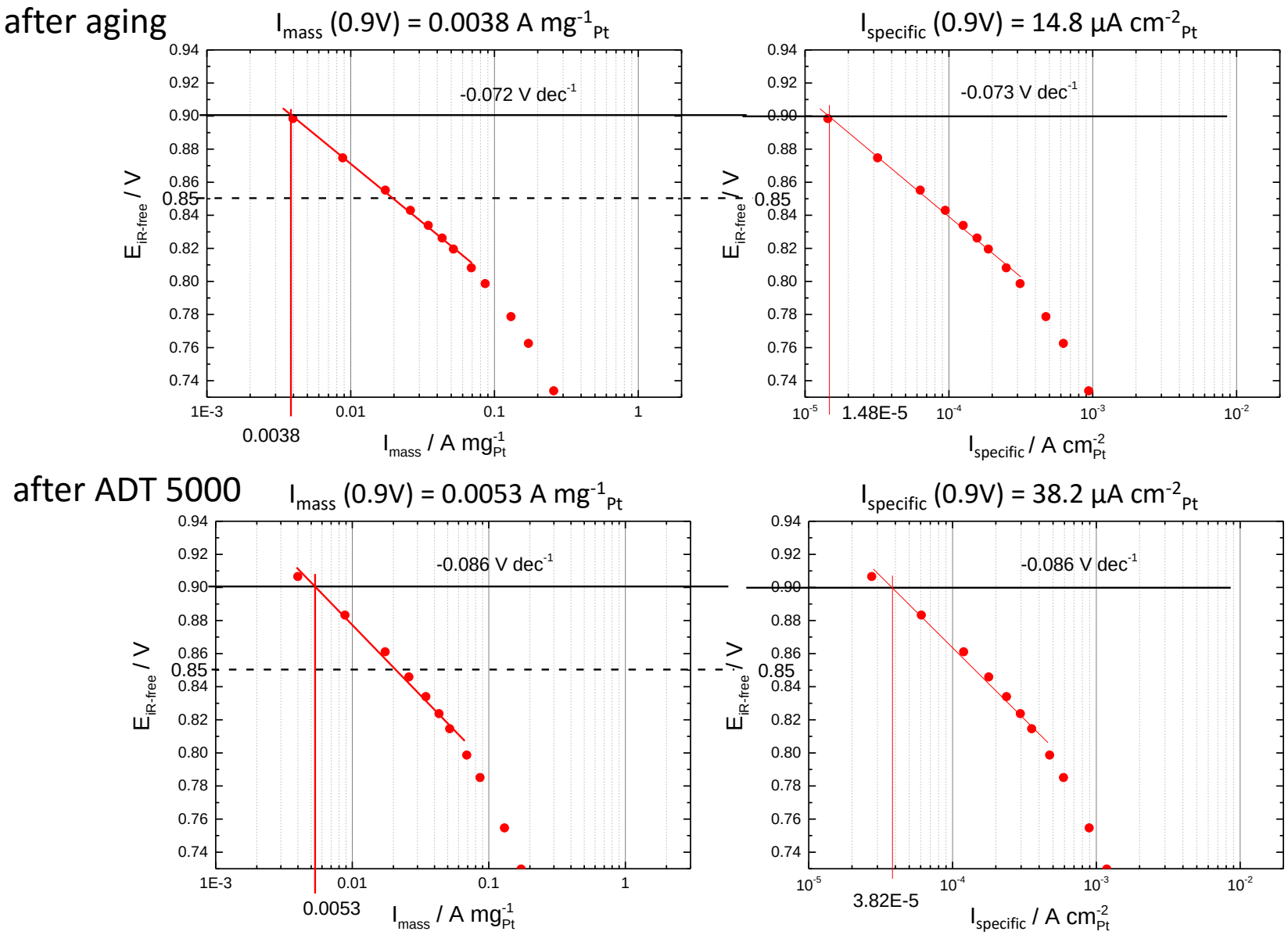

Figure S5. Mass activities and surface specific activities for MEA Pt/MWCNT after the conditioning (activating) and ADT 5000 cycles by semi-logarithmic plots of I-V polarization curves.

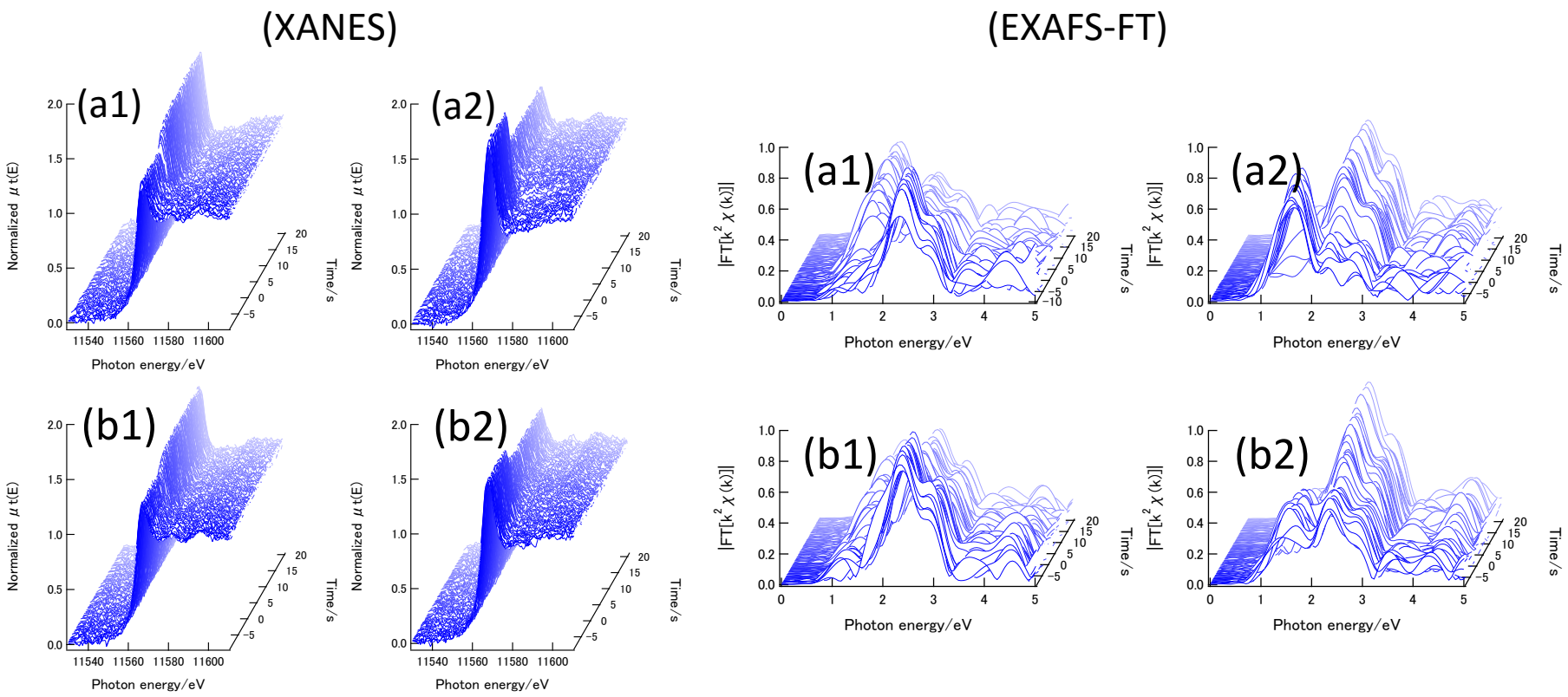

Figure S6. The series of *in situ* time-resolved Pt L_{III}-edge QXANES spectra (every 100 ms) and QEXAFS Fourier transforms (every 300 ms) for Pt/KB after the conditioning (activating) (a) and ADT 1000 cycles (b) in the potential jump operations under H_2(anode)-N_2(cathode). (1) 0.4 V_{RHE} → 1.4 V_{RHE} and (2) 1.4 V_{RHE}→ 0.4 V_{RHE}.

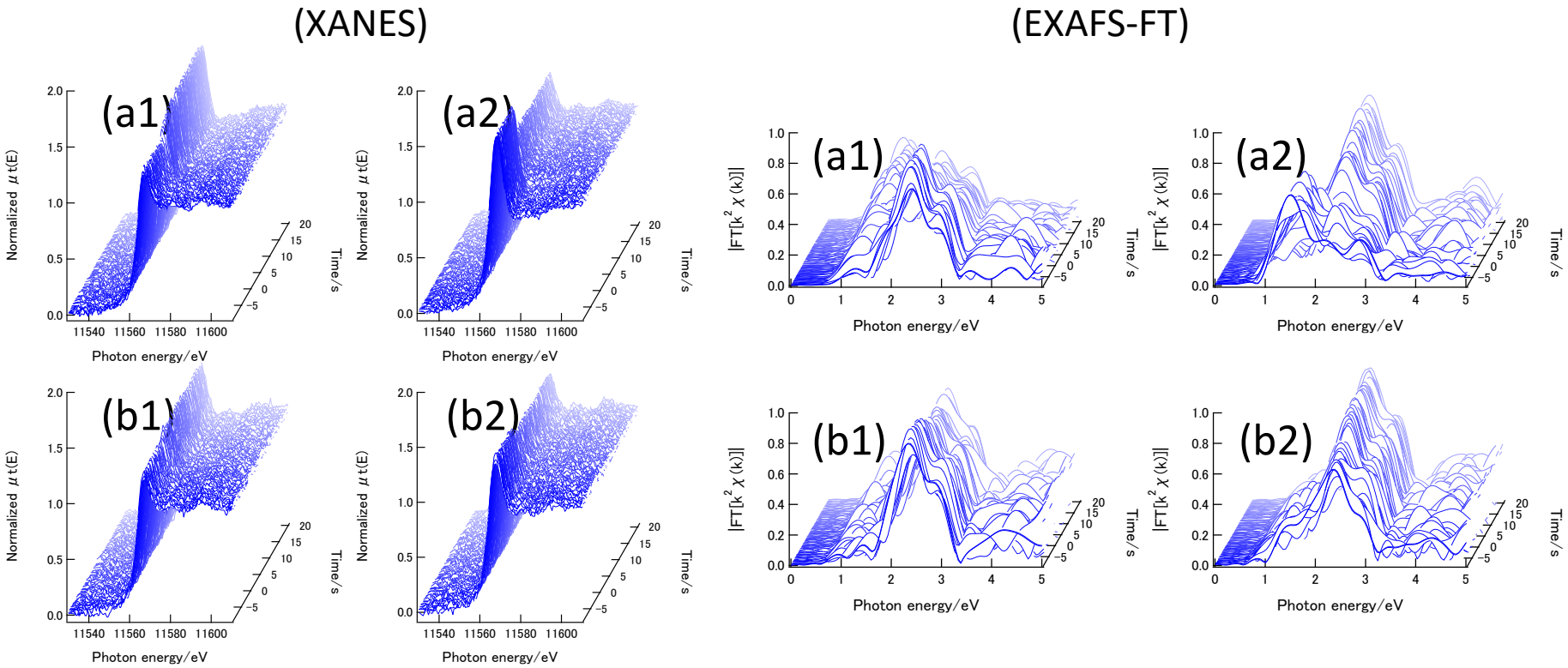

Figure S7. The series of *in situ* time-resolved Pt L_{III}-edge QXANES spectra (every 100 ms) and QEXAFS Fourier transforms (every 300 ms) for Pt/AB after the conditioning (activating) (a) and ADT 5000 cycles (b) in the potential jump operations under H_2(anode)-N_2(cathode). (1) 0.4 V_{RHE} → 1.4 V_{RHE} and (2) 1.4 V_{RHE} → 0.4 V_{RHE}.

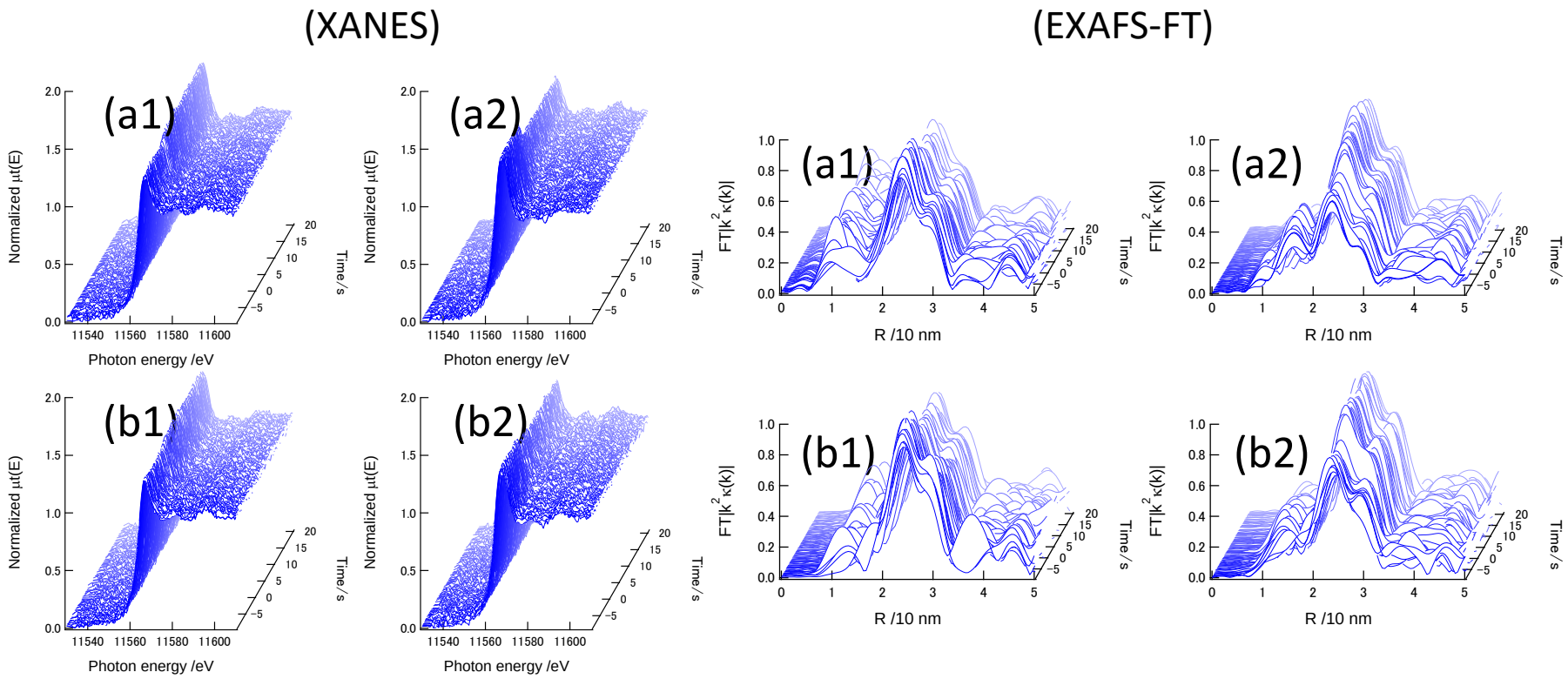

Figure S8. The series of *in situ* time-resolved Pt L_{III}-edge QXANES spectra (every 100 ms) and QEXAFS Fourier transforms (every 300 ms) for Pt/MWCNT after the conditioning (activating) (a) and ADT 5000 cycles (b) in the potential jump operations under H_2(anode)-N_2(cathode). (1) 0.4 V_{RHE} → 1.4 V_{RHE} and (2) 1.4 V_{RHE} → 0.4 V_{RHE}.

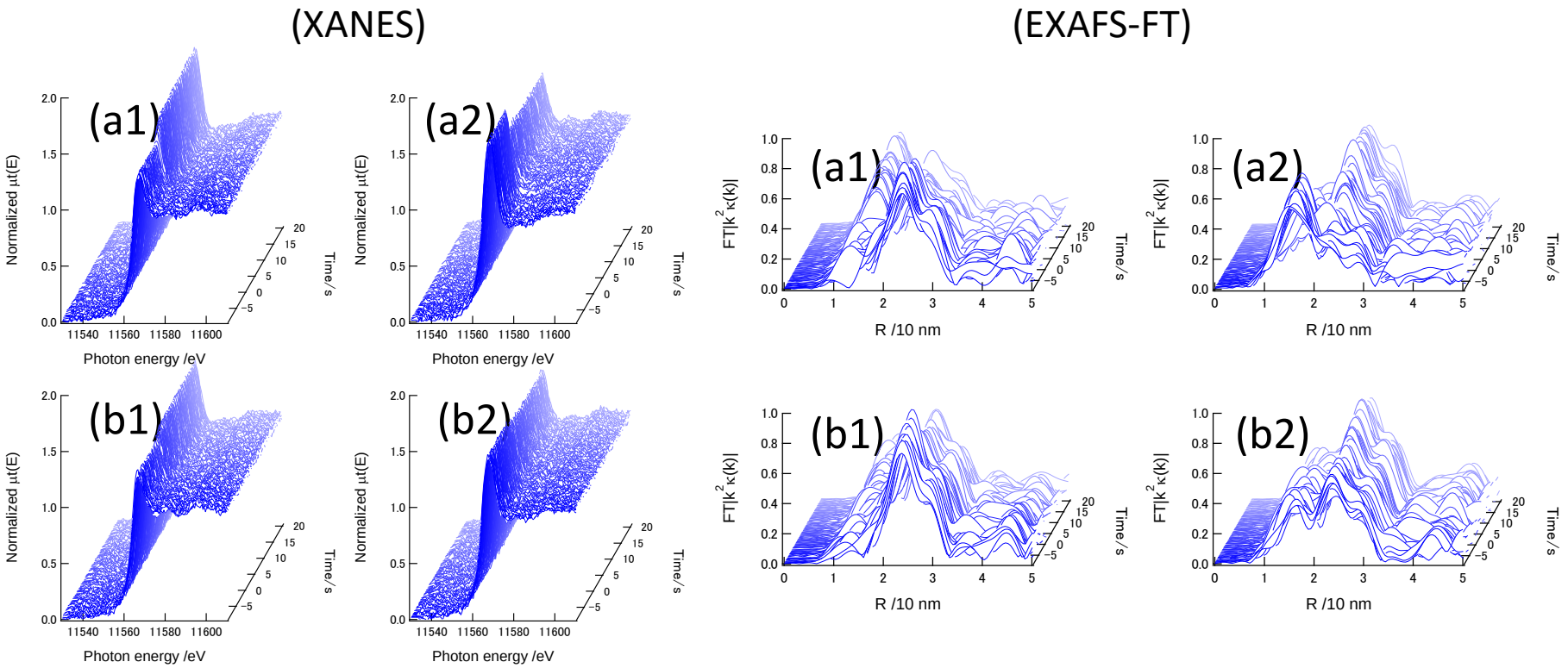

Figure S9. The series of *in situ* time-resolved Pt L_{III}-edge QXANES spectra (every 100 ms) and QEXAFS Fourier transforms (every 300 ms) for Pt/KB after the conditioning (activating) (a) and ADT 1000 cycles (b) in the potential jump operations under H_2(anode)-air(cathode). (1) 0.4 V_{RHE} → 1.4 V_{RHE} and (2) 1.4 V_{RHE} → 0.4 V_{RHE}.

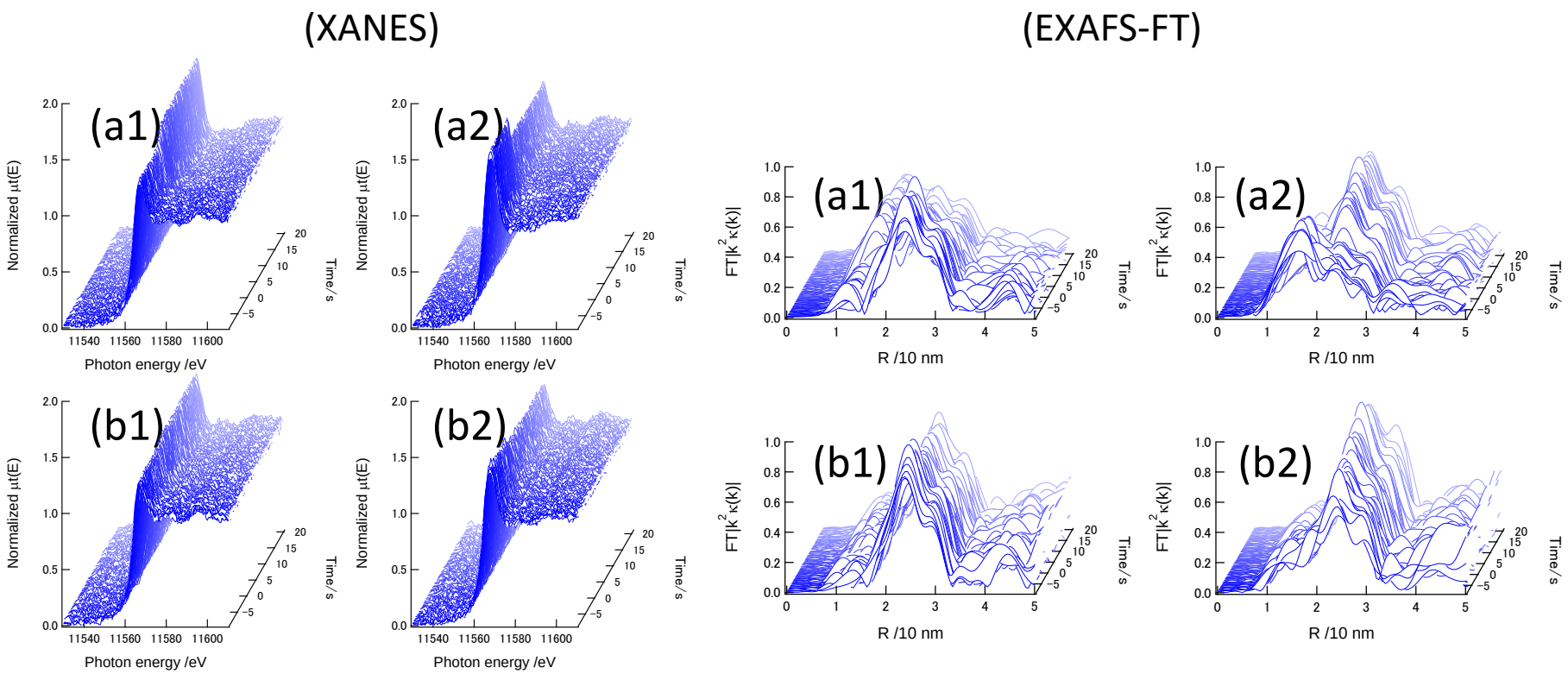

Figure S10. The series of *in situ* time-resolved Pt L_{III}-edge QXANES spectra (every 100 ms) and QEXAFS Fourier transforms (every 300 ms) for Pt/AB after the conditioning (activating) (a) and ADT 5000 cycles (b) in the potential jump operations under H_2(anode)-air(cathode). (1) 0.4 V_{RHE} → 1.4 V_{RHE} and (2) 1.4 V_{RHE} → 0.4 V_{RHE}.

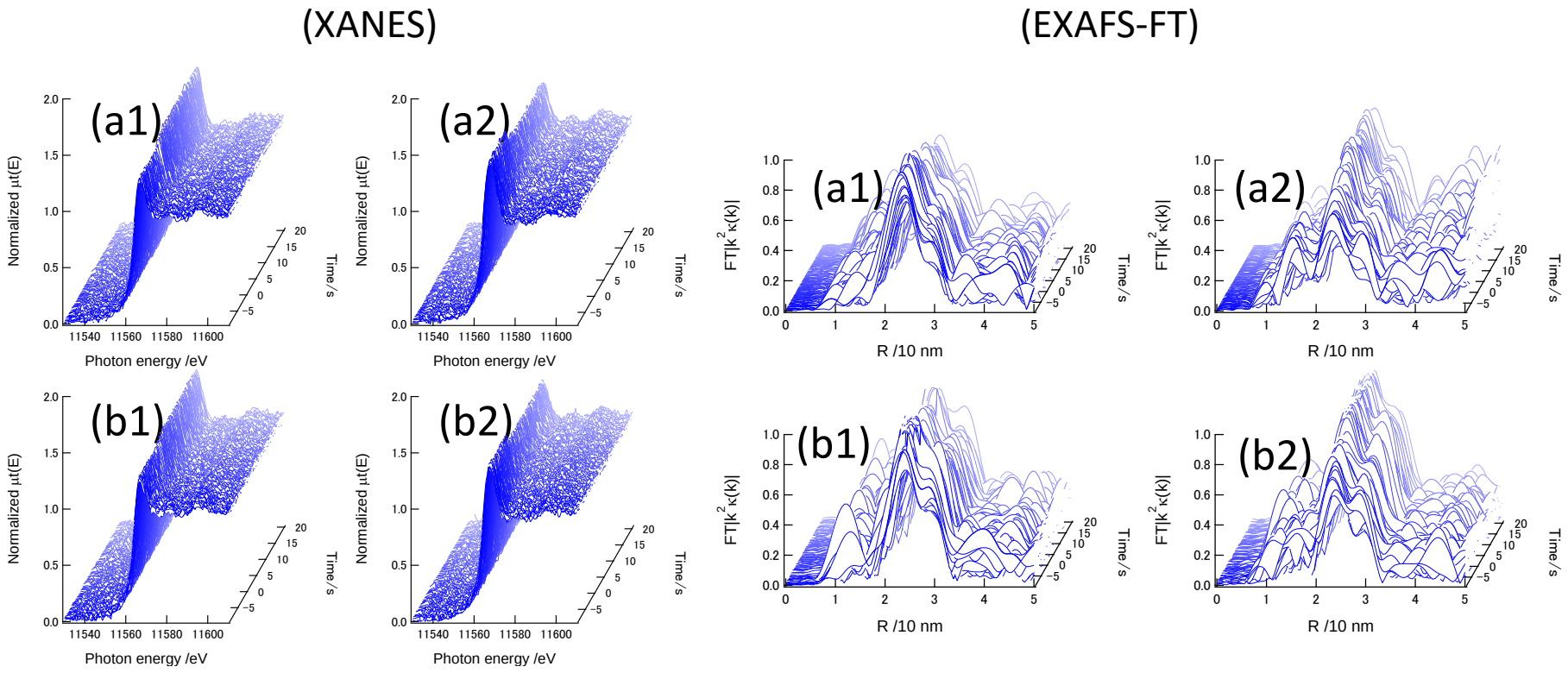

Figure S11. The series of *in situ* time-resolved Pt L_{III}-edge QXANES spectra (every 100 ms) and QEXAFS Fourier transforms (every 300 ms) for Pt/MWCNT after the conditioning (activating) (a) and ADT 5000 cycles (b) in the potential jump operations under H_2(anode)-air(cathode). (1) 0.4 V_{RHE} → 1.4 V_{RHE} and (2) 1.4 V_{RHE} → 0.4 V_{RHE}.

$$\mu t = \frac{a_0}{1+\left(\frac{x-a_1}{a_2}\right)^2} + b_0 \tan^{-1}\left(\frac{(x-b_1)}{b_2} + \frac{\pi}{2}\right) + c \qquad (SI-1)$$

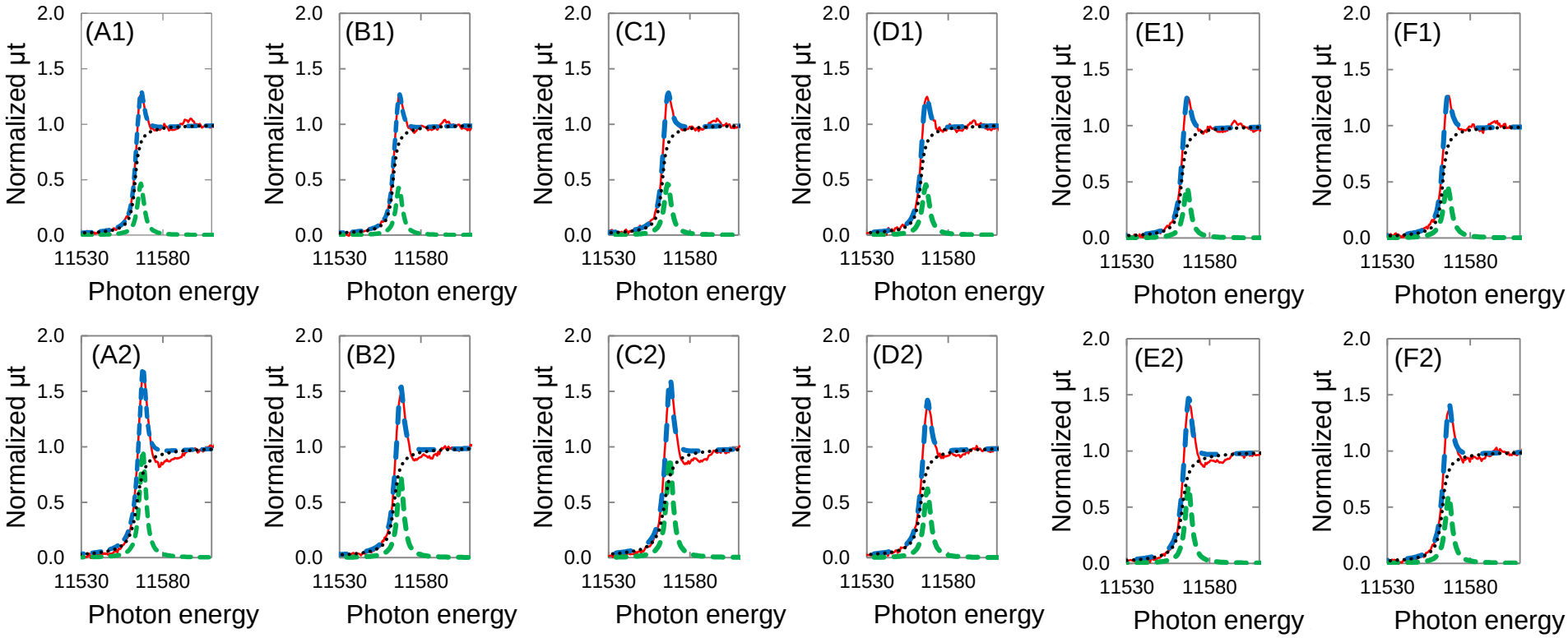

Figure S12. *In situ* Pt L_{III}-edge QXANES spectra (100 ms x 3; solid) at 0.4 V_{RHE} (1) and 1.4 V_{RHE} (2) with the Lorentzian-arctangent fitting curves (dashed) by eq. (S1) for Pt/C cathodes under H_2 (anode) - N_2 (cathode) flows. (A) Pt/KB activated, (B) Pt/KB ADT 1000, (C) Pt/AB activated, (D) Pt/AB ADT 5000, (E) Pt/MWCNT activated, and (F) Pt/MWCNT ADT 5000.

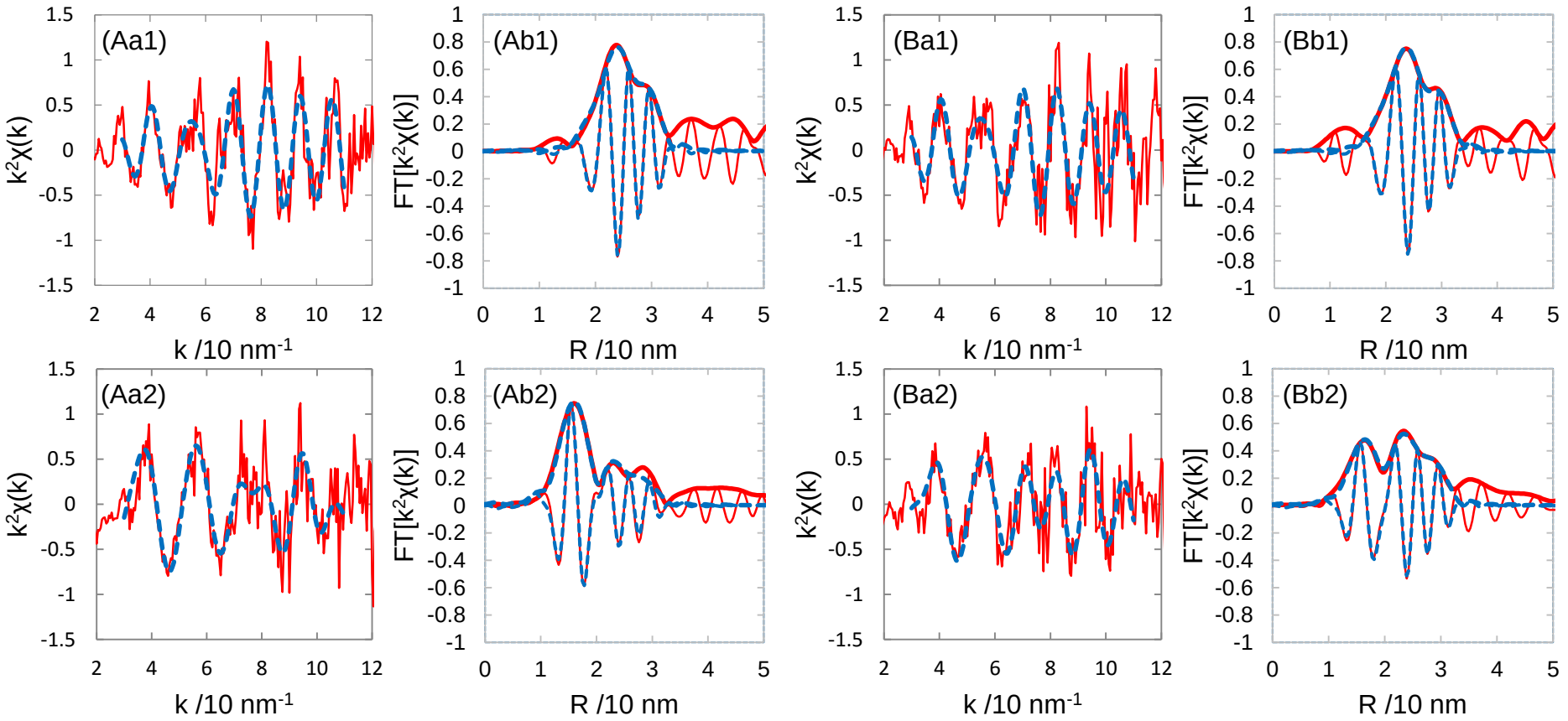

Figure S13. k^2-weighted Pt L_{III}-edge QEXAFS oscillations (a) and their associated Fourier transforms (b) (100 ms x3, merged) for Pt/KB after the conditioning (activating) (A) and ADT 1000 cycles (B) at 0.4 V_{RHE} (1) and 1.4 V_{RHE} (2) under H_2 (anode) -N_2 (cathode) flow. Fitting curves: dashed; Fitting ranges: 30 – 110 nm^{-1} for Δk and 0.13 – 0.32 nm for ΔR.

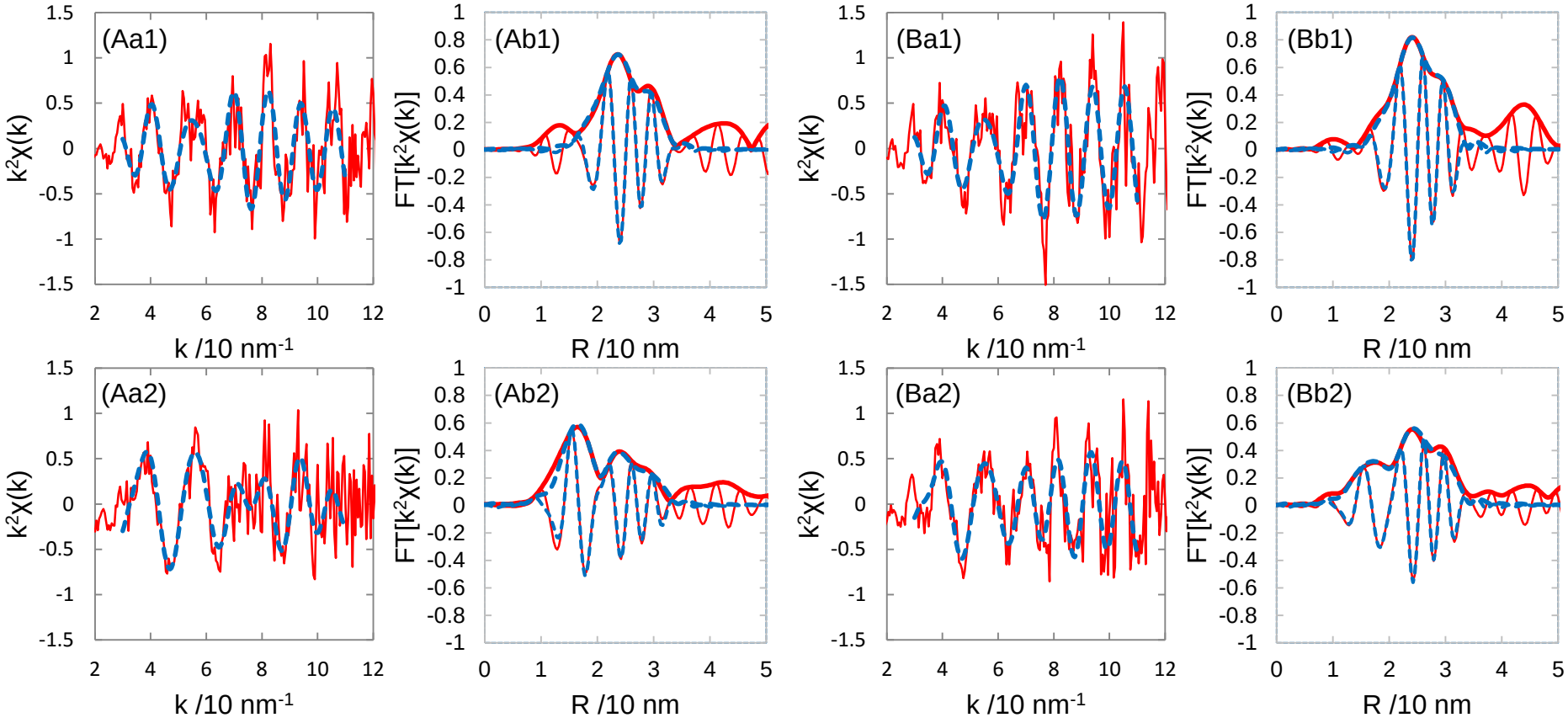

Figure S14. k^2-weighted Pt L_{III}-edge QEXAFS oscillations (a) and their associated Fourier transforms (b) (100 ms x3, merged) for Pt/AB after the conditioning (activating) (A) and ADT 5000 cycles (B) at 0.4 V_{RHE} (1) and 1.4 V_{RHE} (2) under H_2 (anode) -N_2 (cathode) flow. Fitting curves: dashed; Fitting ranges: 30 – 110 nm^{-1} for Δk and 0.13 – 0.32 nm for ΔR.

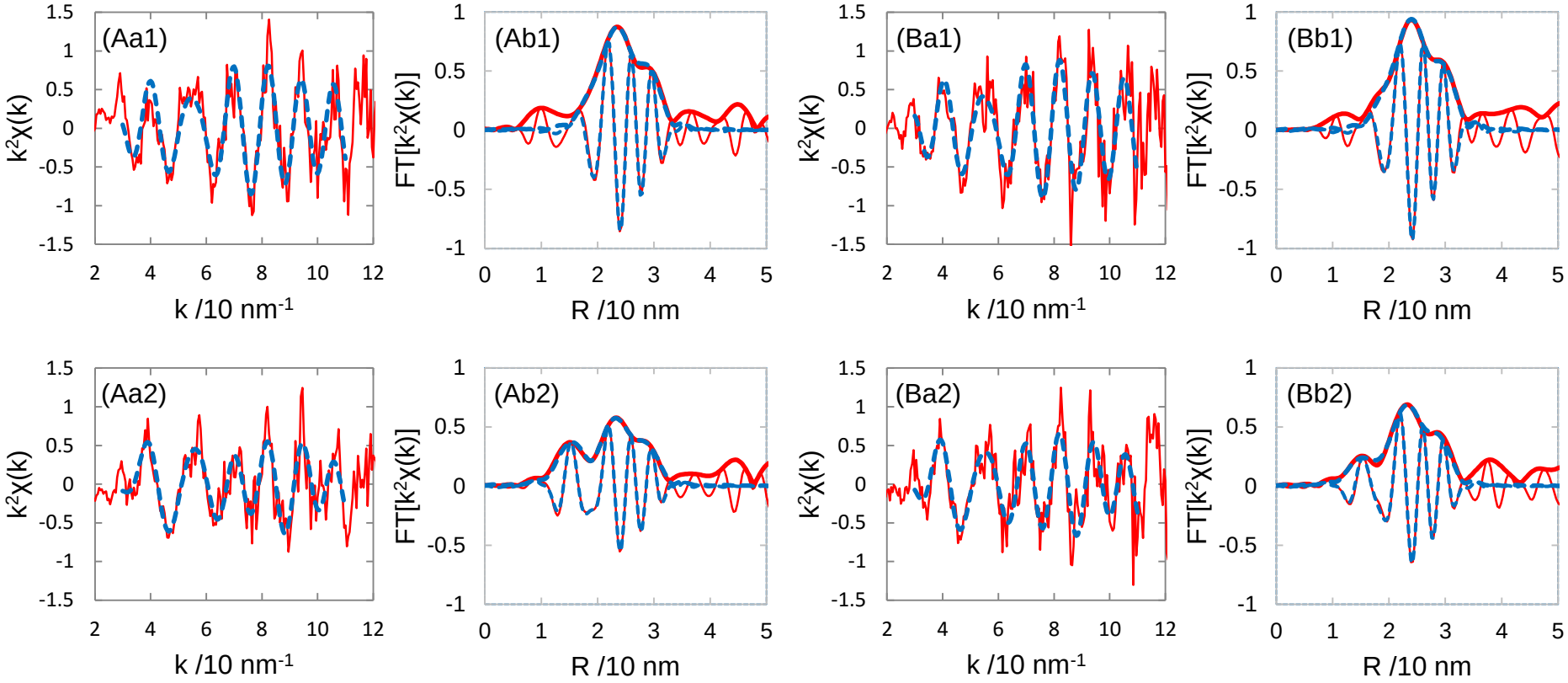

Figure S15. (same as Figure 3)**.** k^2-weighted Pt L_{III}-edge QEXAFS oscillations (a) and their associated Fourier transforms (b) (100 ms x3, merged) for Pt/MWCNT after the conditioning (activating)(A) and ADT 5000 cycles (B) at 0.4 V_{RHE} (1) and 1.4 V_{RHE} (2) under H_2 (anode) -N_2 (cathode) flow. Fitting curves: dashed; Fitting ranges: 30 – 110 nm^{-1} for Δk and 0.13 – 0.32 nm for ΔR.

Table S1. Curve-fitting results of the k^2-weighted QEXAFS data for Pt/KB, Pt/AB, and Pt/MWCNT in activated and ADT-degraded MEAs in H_2-Air

(1) Pt/KB (activated)

Potential/V_{RHE}	Bond	CN	σ^2 / 10^{-4}nm^2	E_0 / eV	R / nm	R_f / %
0.4	Pt-Pt	9.3 ± 0.9	0.629 ± 0.077	4.5 ± 1.0	0.275 ± 0.001	0.2
	Pt-O	0.5 ± 0.6	1.302 ± 1.103		0.201 ± 0.003	
1.4	Pt-Pt	5.0 ± 1.2	0.689 ± 0.192	3.4 ± 1.2	0.274 ± 0.001	0.4
	Pt-O	1.7 ± 0.3	0.426 ± 0.169		0.200 ± 0.001	

(2) Pt/KB (ADT 1000)

Potential/V_{RHE}	Bond	CN	σ^2 / 10^{-4}nm^2	E_0 / eV	R / nm	R_f / %
0.4	Pt-Pt	10.7 ± 1.2	0.711 ± 0.090	4.6 ± 1.4	0.276 ± 0.001	0.4
	Pt-O	0.3 ± 0.4	0.381 ± 1.705		0.212 ± 0.006	
1.4	Pt-Pt	7.2 ± 1.4	0.765 ± 0.163	3.0 ± 1.4	0.274 ± 0.001	0.7
	Pt-O	1.2 ± 0.4	0.303 ± 0.329		0.199 ± 0.001	

(3) Pt/AB (activated)

Potential/V_{RHE}	Bond	CN	σ^2 / 10^{-4}nm^2	E_0 / eV	R / nm	R_f / %
0.4	Pt-Pt	10.0 ± 1.3	0.650 ± 0.103	5.5 ± 1.6	0.277 ± 0.001	0.5
	Pt-O	0.3 ± 0.4	0.075 ± 1.218		0.213 ± 0.004	
1.4	Pt-Pt	5.4 ± 1.0	0.800 ± 0.156	4.5 ± 1.1	0.275 ± 0.001	0.3
	Pt-O	1.5 ± 0.3	0.648 ± 0.175		0.201 ± 0.001	

(4) Pt/AB (ADT 5000)

Potential/V_{RHE}	Bond	CN	σ^2 / 10^{-4}nm^2	E_0 / eV	R / nm	R_f / %
0.4	Pt-Pt	10.3 ± 1.0	0.655 ± 0.070	4.9 ± 1.1	0.276 ± 0.001	0.2
	Pt-O	0.3 ± 0.7	1.249 ± 6.189		0.205 ± 0.017	
1.4	Pt-Pt	9.5 ± 1.4	0.690 ± 0.117	3.9 ± 1.2	0.276 ± 0.001	0.4
	Pt-O	0.7 ± 0.4	0.353 ± 0.466		0.201 ± 0.002	

(5) Pt/MWCNT (activated)

Potential/V_{RHE}	Bond	CN	σ^2 / 10^{-4}nm^2	E_0 / eV	R / nm	R_f / %
0.4	Pt-Pt	10.7 ± 0.9	0.716 ± 0.062	5.7 ± 0.8	0.277 ± 0.001	0.1
	Pt-O	0.2 ± 0.3	0.607 ± 1.508		0.204 ± 0.005	
1.4	Pt-Pt	8.5 ± 0.7	0.683 ± 0.069	2.5 ± 0.7	0.274 ± 0.001	0.1
	Pt-O	0.9 ± 0.2	0.349 ± 0.247		0.200 ± 0.001	

(6) Pt/MWCNT (ADT 5000)

Potential/V_{RHE}	Bond	CN	σ^2 / 10^{-4}nm^2	E_0 / eV	R / nm	R_f / %
0.4	Pt-Pt	10.1 ± 1.7	0.540 ± 0.132	6.5 ± 1.5	0.277 ± 0.001	0.7
	Pt-O	0.3 ± 0.5	0.367 ± 1.386		0.202 ± 0.005	
1.4	Pt-Pt	8.1 ± 1.4	0.581 ± 0.127	4.6 ± 1.4	0.275 ± 0.001	0.6
	Pt-O	0.9 ± 0.6	0.794 ± 0.938		0.199 ± 0.003	

Effect of k-range on the EXAFS analysis

The analysis results for k-range 3-12 $Å^{-1}$ are almost the same as those for k-range 3-11 $Å^{-1}$ within error range. The analysis results for k-range 3-13 $Å^{-1}$ are also similar to those for k-range 3-11 $Å^{-1}$, but the R-factor becomes larger, indicating totally worse fitting. Nevertheless, among lots of time-resolved XAFS data under fuel cell operating conditions, there were the samples, which were hard to measure good XAFS signals in the larger region than 120 nm^{-1}, particularly with degraded (ADT) samples. In this study we systematically compared the potential-dependent structures and electronic states and transient response structural and electronic transformations of typical three Pt/C catalysts (Pt/KB, Pt/AB and Pt/MWCNT) at 100 ms (or 100 ms x3) time-resolution, and for quantitative comparison we conducted the fitting procedures under the same analysis conditions. Hence, the k-ranges for all lots of the potential-dependent and transient-response data were unified as 3-11 $Å^{-1}$ in this study.

Comparison between the EXAFS analysis results with different k-ranges in $Å^{-1}$ for activated Pt/KB at 0.4 V (R-range = 1.3 – 3.2 Å)

	k=2-11	k=3-11	k=2-12	k=3-12	k=3-13
CN(Pt-Pt)	10.4 ± 0.7	10.0 ± 0.7	10.8 ± 0.8	10.7 ± 0.95	10.2 ± 1.4
dE_0 / eV	5.10 ± 0.59	5.09 ± 0.89	4.96 ± 0.75	4.82 ± 1.12	5.18 ± 1.55
R(Pt-Pt) / Å	2.75 ± 0.005	2.75 ± 0.01	2.75 ± 0.005	2.75 ± 0.01	2.75 ± 0.01
σ^2 / $Å^{-2}$	0.0056 ± 0.0006	0.0054 ± 0.0007	0.0062 ± 0.0006	0.0063 ± 0.0007	0.0074 ± 0.0009
R-factor / %	0.43	0.46	0.79	0.91	2.25

Estimation of the EXAFS data for the Pt/C catalysts after the ADT cycles

The Pt nanoparticles in Pt/KB, Pt/AB and Pt/MWCNT grew to 6.5 nm ±1.5 nm (~14 Pt layers) after the ADT cycles. Thus, the CN(Pt-Pt) at 0.4 V_{RHE} is expected to be 11.4 by the equation $(12*(1^2+2^2+3^2+4^2+5^2+6^2+7^2+8^2+9^2+10^2+11^2+12^2+13^2)+9*14^2)/(1^2+2^2+3^2+4^2+5^2+6^2+7^2+8^2+9^2+10^2+11^2+12^2+13^2+14^2)$, which reproduces the observed CN(Pt-Pt) values under H_2 (anode) - N_2 (cathode) (the values under H_2 (anode) - Air (cathode) in bracket); 11.0 ±1.4 (10.7 ±1.2), 10.3 ±0.9 (10.3 ±1.0) and 11.0 ± 0.8 (10.1 ± 1.7), respectively for Pt/KB (ADT 1000), Pt/AB (ADT 5000) and Pt/MWCNT (ADT 5000) (Table 2 and Table S1). At 1.4 V_{RHE}, the CN(Pt-Pt) and CN(Pt-O) are expected to be 9.4 and 1.1 by the equations $12*(1^2+2^2+3^2+4^2+5^2+6^2+7^2+8^2+9^2+10^2+11^2+12^2)*1/(1^2+2^2+3^2+4^2+5^2+6^2+7^2+8^2+9^2+10^2+11^2+12^2+13^2+14^2)+ 9*13^2*1/(1^2+2^2+3^2+4^2+5^2+6^2+7^2+8^2+9^2+10^2+11^2+12^2+13^2+14^2)$ and $(14^2*1*4+13^2*1*2)/(1^2+2^2+3^2+4^2+5^2+6^2+ 7^2+ 8^2+9^2+10^2+11^2+12^2+13^2+14^2)$, respectively, which also totally reproduce the observed CN(Pt-Pt) and CN(Pt-O) values under H_2 (anode) - N_2 (cathode) (under H_2 (anode) - Air (cathode) in bracket); 6.5 ±1.0 (7.2 ±1.4) and 1.3 ±0.4 (1.2 ±0.4), 8.8 ±1.9 (9.5 ±1.4) and 0.7 ±0.6 (0.7 ±0.4), and 8.4 ±1.2 (8.1 ±1.4) and 0.9 ±0.4 (0.9 ±0.6), respectively for Pt/KB (ADT 1000), Pt/AB (ADT 5000) and Pt/MWCNT (ADT 5000). The smaller CN(Pt-Pt) may indicate some distortion at the13^{th} Pt layer underneath the PtO phase. These results reveal the similar surface structures of Pt nanoparticles under both cathode gas conditions at 0.4 V_{RHE} and 1.4 V_{RHE} (Figure 4) except the partial presence of surface oxygen species at 0.4 V_{RHE} under H_2 (anode) - Air (cathode).

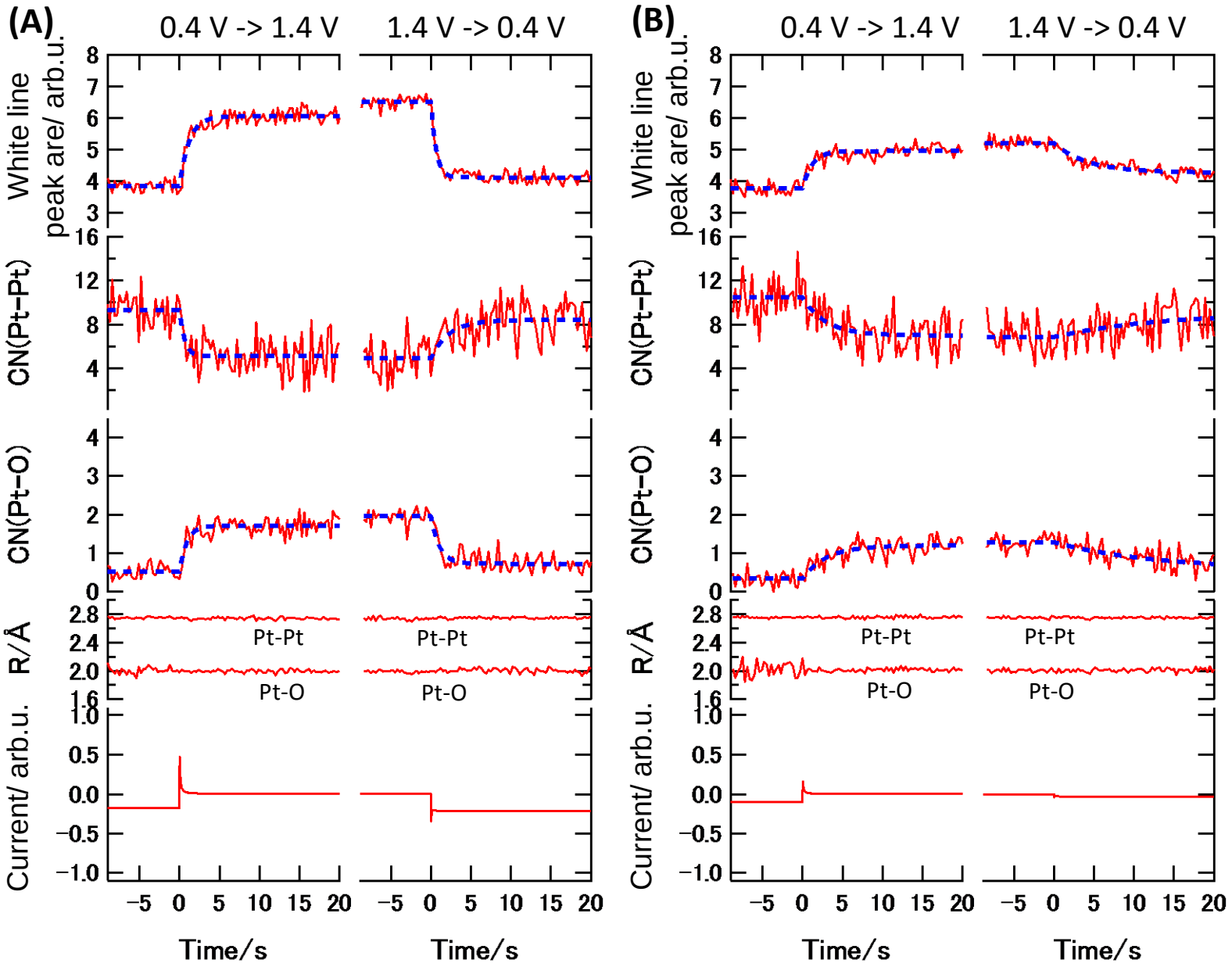

Figure S16. Transient response curves of the white line intensity, CN(Pt-Pt), CN(Pt-O), R(Pt-Pt), R(Pt-O), and current for Pt/KB after the conditioning (activating) (A) and ADT 1000 cycles (B) in the voltage up (0.4 V_{RHE} -→ 1.4 V_{RHE}) and down (1.4 V_{RHE} -→ 0.4 V_{RHE}) cycle under H_2(anode)-Air(cathode); Cell temp.: 353 K, Relative humidity: ~ 93%.

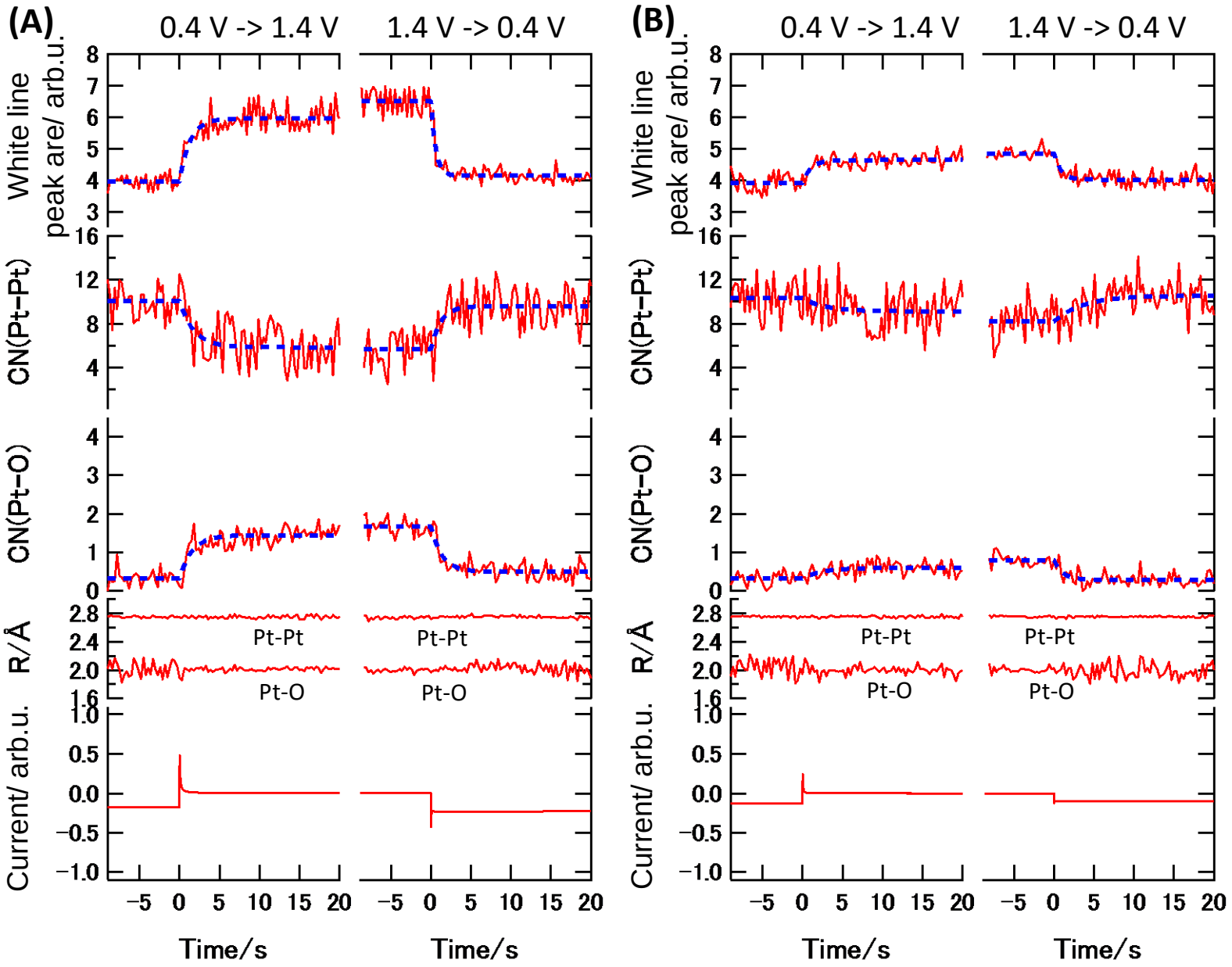

Figure S17. Transient response curves of the white line intensity, CN(Pt-Pt), CN(Pt-O), R(Pt-Pt), R(Pt-O), and current for Pt/AB after the conditioning (activating) (A) and ADT 5000 cycles (B) in the voltage up (0.4 V_{RHE} -→ 1.4 V_{RHE}) and down (1.4 V_{RHE} -→ 0.4 V_{RHE}) cycle under H_2(anode)-Air(cathode); Cell temp.: 353 K, Relative humidity: ~ 93%.

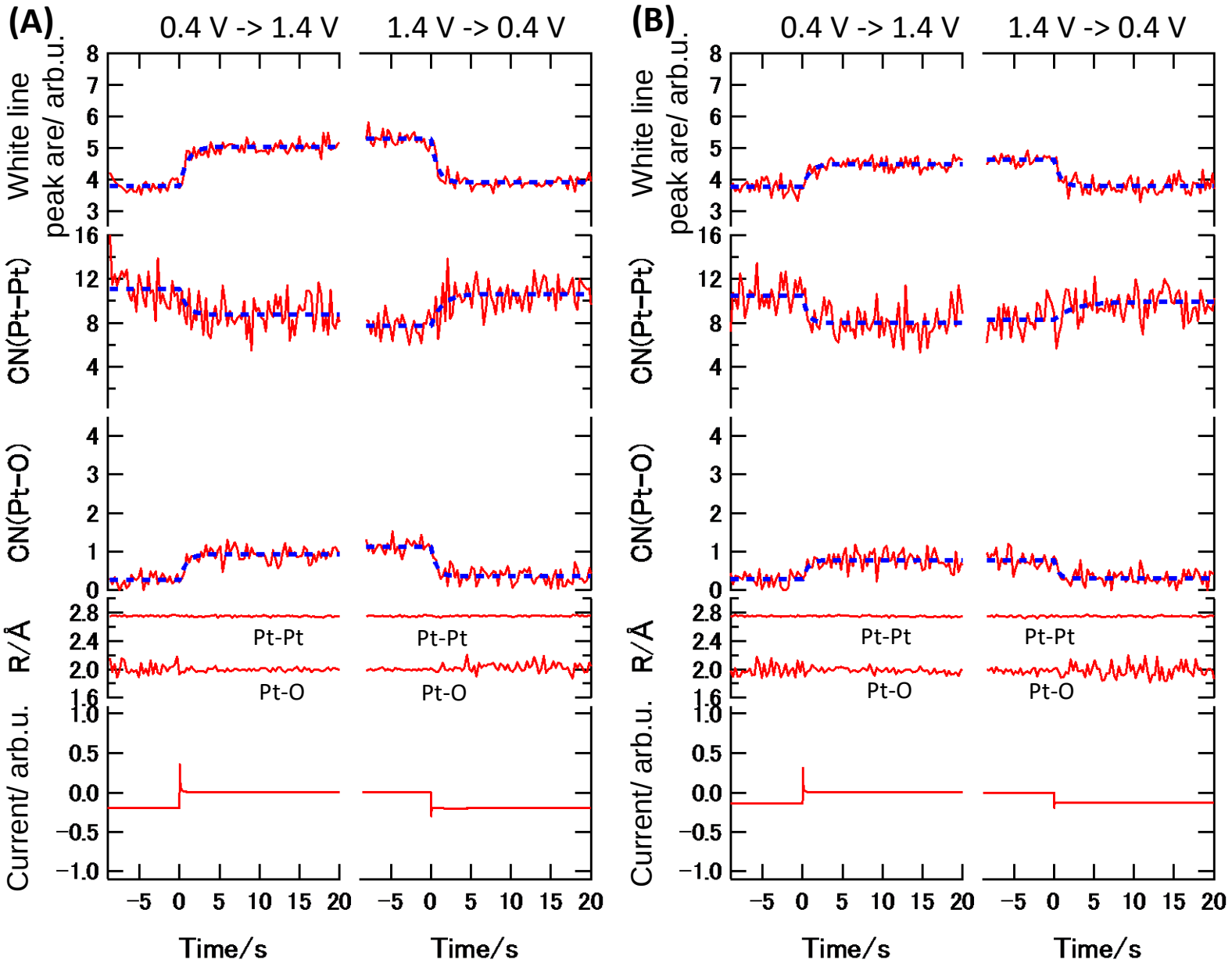

Figure S18. Transient response curves of the white line intensity, CN(Pt-Pt), CN(Pt-O), R(Pt-Pt), R(Pt-O), and current for Pt/MWCNT after the conditioning (activating) (A) and ADT 5000 cycles (B) in the voltage up (0.4 V_{RHE} -→ 1.4 V_{RHE}) and down (1.4 V_{RHE} -→ 0.4 V_{RHE}) cycle under H_2(anode)-Air(cathode); Cell temp.: 353 K, Relative humidity: ~ 93%.

Table S2. Tentative rate constants (k and k') for the electrochemical reactions and the electronic (Pt valence) and structural (CN(Pt-Pt) and CN(Pt-O)) changes in Pt/KB, Pt/AB and Pt/MWCNT after the conditioning (activating) and ADT cycles in the potential operations under H_2(anode)-Air(cathode); Cell temp.: 353 K, Relative humidity: ~ 93%

	Pt/KB		Pt/AB		Pt/MWCNT	
	activated	ADT1000	activated	ADT5000	activated	ADT5000
$k_{valence}$ (1) and $k'_{valence}$ (2)						
(1) 0.4 V -> 1.4 V	0.85 ± 0.0768[a)]	0.842 ± 0.126[a)]	0.769 ± 0.121[a)]	0.957 ± 0.317[a)]	0.987 ± 0.168[a)]	1.08 ± 0.351[a)]
(2) 1.4 V -> 0.4 V	1.61 ± 0.175[a)]	0.238 ± 0.035[a)]	1.71 ± 0.318[a)]	1.17 ± 0.363[a)]	1.25 ± 0.211[a)]	1.35 ± 0.425[a)]
k_{Pt-Pt} (1) and k'_{Pt-Pt} (2)						
(1) 0.4 V -> 1.4 V	1.6 ± 0.853[a)]	0.342 ± 0.129[a)]	0.554 ± 0.203[a)]	0.361 ± 0.419[a)]	1.14 ± 0.989[a)]	1.65 ± 1.28[a)]
(2) 1.4 V -> 0.4 V	0.449 ± 0.178[a)]	0.0791 ± 0.105[a)]	0.811 ± 0.368[a)]	0.283 ± 0.162[a)]	0.718 ± 0.336[a)]	0.406 ± 0.278[a)]
k_{Pt-O} (1) and k'_{Pt-O} (2)						
(1) 0.4 V -> 1.4 V	1.1 ± 0.217[a)]	0.333 ± 0.0632[a)]	0.634 ± 0.114[a)]	0.427 ± 0.216[a)]	1.17 ± 0.36[a)]	1.45 ± 0.745[a)]
(2) 1.4 V -> 0.4 V	0.942 ± 0.171[a)]	0.0825 ± 0.0408[a)]	0.722 ± 0.131[a)]	0.917 ± 0.329[a)]	1.52 ± 0.458[a)]	2.05 ± 1.35[a)]
k_e (1) and k'_e (2)						
(1) 0.4 V -> 1.4 V	13.1 ± 0.0989[b)]	13.3 ± 0.123[b)]	16.7 ± 0.169[b)]	22.5 ± 0.153[b)]	32.1 ± 0.243[b)]	29.7 ± 0.255[b)]
	1.81 ± 0.0214[b)]	1.57 ± 0.0152[b)]	2.03 ± 0.0263[b)]	2.65 ± 0.0308[b)]	1.35 ± 0.18[b)]	0.425 ± 0.355[b)]
(2) 1.4 V -> 0.4 V	22.6 ± 0.438[b)]	(59.0)	36.4 ± 0.663[b)]	(48.2)[b)c)]	8.05 ± 1.34[b)]	(72.8)[b)c)]
	1.88 ± 0.0651[b)]	0.263 ± 0.0114[b)]	2.3 ± 0.194[b)]	0.416 ± 0.0101[b)]	1.48 ± 0.292[b)]	0.153 ± 0.0987[b)]

[a)] XAFS acquisition: every 300 ms. [b)] Current acquisition: every 20 ms. [C)] tentative with large error bar.

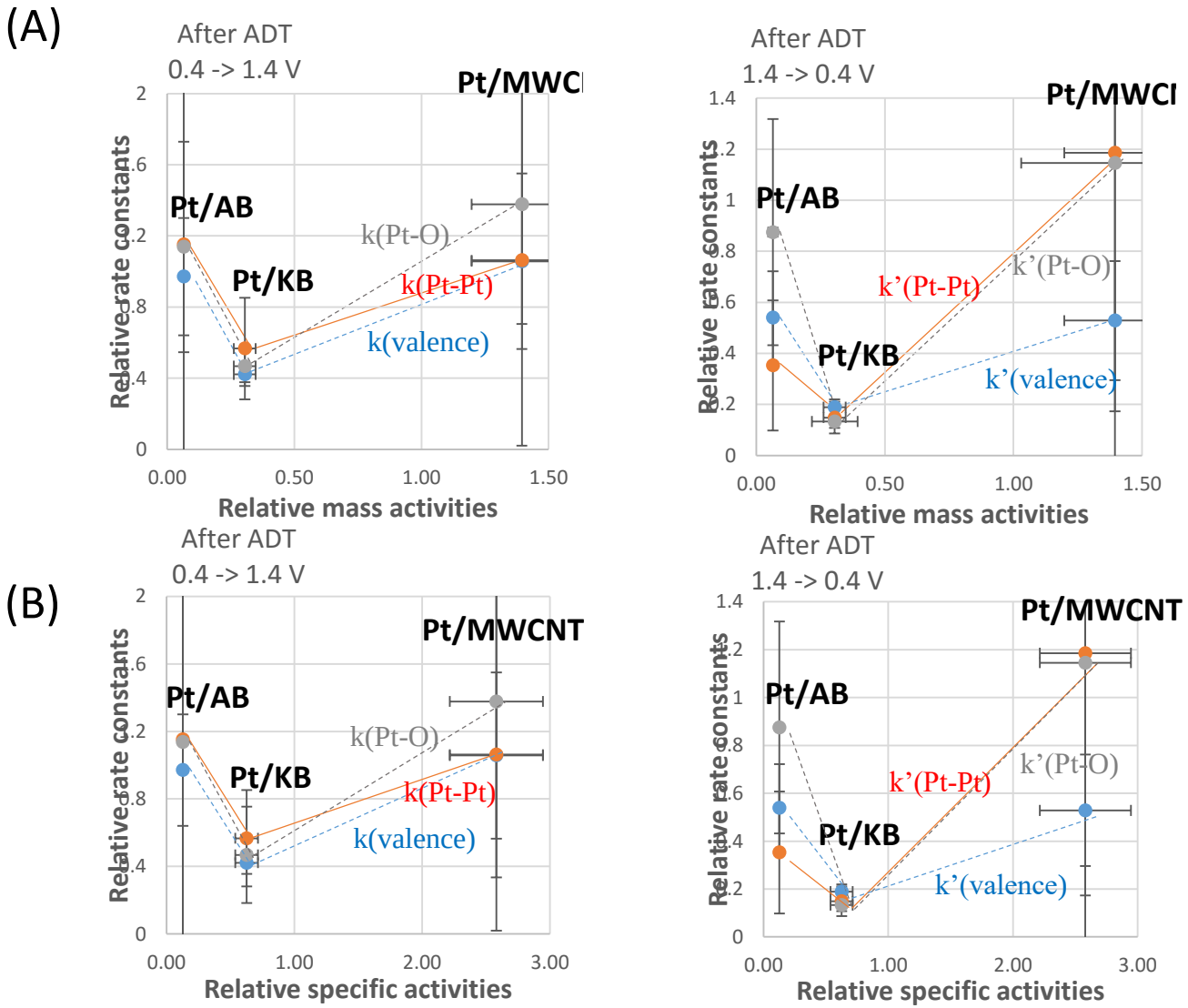

Figure S19. The dependence of the relative rate constants and relative mass activities (A) or surface specific activities (B) for the Pt/KB, Pt/AB and Pt/MWCNT cathodes in MEAs after ADT cycles. The relative rate constants k(valence), k(Pt-Pt) and k(Pt-O), and k'(valence), k'(Pt-Pt) and k'(Pt-O) for each sample after the ADT cycles are the relative values to those for each corresponding activated sample, respectively. The relative mass activities and surface specific activities for each sample after the ADT cycles are the relative values to those for each corresponding activated sample.

The error range for the ratio k`/k was calculated by the following equation.

$$m = y \pm \Delta y, \qquad n = x \pm \Delta x \tag{SI-2}$$

$$\frac{m}{n} = (y \pm \Delta y)/x \pm \Delta x) = (m/n) \pm \sqrt{\left(\frac{\Delta x}{x}\right)^2 + \left(\frac{\Delta y}{y}\right)^2} \tag{SI-3}$$